Infrared Topological Plasmons in Graphene

Dafei Jin,[1,*] Thomas Christensen,[2,†] Marin Soljačić,[2] Nicholas X. Fang,[3] Ling Lu,[4,‡] and Xiang Zhang[1,§]
[1]Department of Mechanical Engineering, University of California, Berkeley, California 94720, USA
[2]Department of Physics, Massachusetts Institute of Technology, Cambridge, Massachusetts 02139, USA
[3]Department of Mechanical Engineering, Massachusetts Institute of Technology, Cambridge, Massachusetts 02139, USA
[4]Institute of Physics, Chinese Academy of Sciences/Beijing National Laboratory for Condensed Matter Physics, Beijing 100190, China
(Received 23 February 2017; published 16 June 2017)

We propose a two-dimensional plasmonic platform—periodically patterned monolayer graphene—which hosts topological one-way edge states operable up to infrared frequencies. We classify the band topology of this plasmonic system under time-reversal-symmetry breaking induced by a static magnetic field. At finite doping, the system supports topologically nontrivial band gaps with mid-gap frequencies up to tens of terahertz. By the bulk-edge correspondence, these band gaps host topologically protected one-way edge plasmons, which are immune to backscattering from structural defects and subject only to intrinsic material and radiation loss. Our findings reveal a promising approach to engineer topologically robust chiral plasmonic devices and demonstrate a realistic example of high-frequency topological edge states.

DOI: 10.1103/PhysRevLett.118.245301

Time-reversal-symmetry ($\mathcal{T}$) breaking, a necessary condition for achieving quantum Hall phases [1,2], has now been successfully implemented in several bosonic systems, as illustrated by the experimental observation of topologically protected one-way edge transport of photons [3,4] and phonons [5]. More generally, two-dimensional (2D) $\mathcal{T}$ broken topological bosonic phases have been proposed in a range of bosonic phases, spanning photons [6], phonons [7,8], magnons [9], excitons [10], and polaritons [11]. The operating frequency of these systems is typically small, however—far below terahertz—limited by the spectral range of the $\mathcal{T}$-breaking mechanism. For example, the gyromagnetic effect employed in topological photonic crystals is limited by the Larmor frequency of the underlying ferrimagnetic resonance, on the order of tens of gigahertz [3]. In phononic realizations, the attainable gyrational frequencies limit operation further still, to the range of kilohertz [12]. Towards optical frequencies, proposals of dynamic index modulation [13] and optomechanical coupling [14] are promising but experimentally challenging to scale to multiple coupled elements [15–17].

Recently, Jin *et al.* [18] pointed out that the well-known magnetoplasmons of uniform 2D electron gases [19,20] constitute an example of a topologically nontrivial bosonic phase hosting unidirectional edge states. However, as the topological gap exists only below the cyclotron frequency ω_c, the spectral operation remains limited to low frequencies. In this Letter, we show that by suitably engineering the plasmonic band structure of a periodically nanostructured 2D monolayer graphene, see Fig. 1(a), the operation frequency of topological plasmons [21] can be raised dramatically, to tens of terahertz, while maintaining large-gap–midgap ratios even under modest **B** fields. Bridging

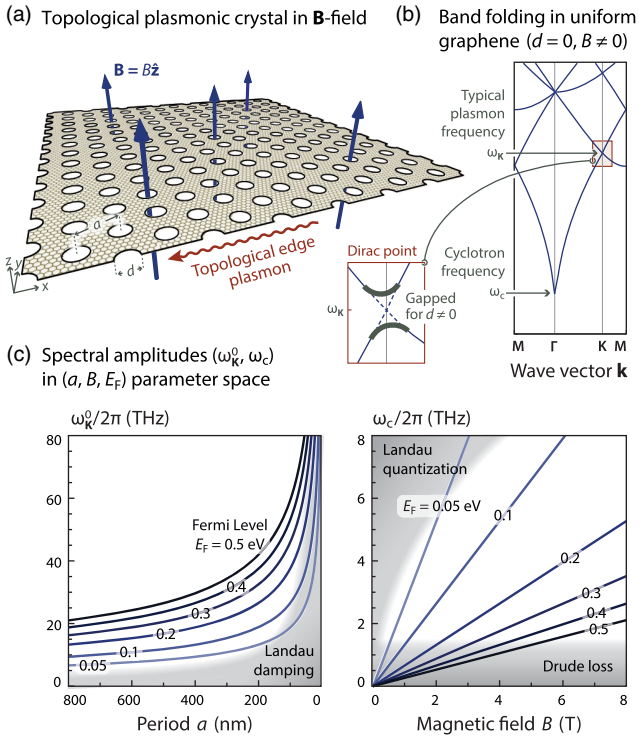

FIG. 1. Two-dimensional topological plasmonic crystal under magnetically induced $\mathcal{T}$ breaking. (a) Schematic of triangular antidot lattice in graphene. Under an external magnetic field $\mathbf{B} = B\hat{\mathbf{z}}$, a finite lattice supports topologically protected one-way edge plasmons. (b) Band-folded plasmon dispersion in uniform graphene at $B \neq 0$; characteristic frequencies $\omega_{\mathbf{K}}$ and ω_c indicated. The symmetry-induced Dirac cone is gapped for $d \neq 0$. (c) Characteristic frequencies' dependence on the crystal period a, magnetic field B, and Fermi level E_F.

ultrafast electronics and infrared topological photonics, the proposed platform can be integrated with CMOS technology, allowing dynamically gate-tunable topological states across a broad spectral range.

Graphene distinguishes itself as an ideal platform for topological plasmonics in three key aspects: first, it supports large, tunable carrier densities $n \sim 10^{11}$–10^{14} cm^{-2} [27–29], or equivalently, large, tunable Fermi energies $E_F = \hbar v_F \sqrt{\pi n}$ (Fermi velocity, $v_F \approx 9.1 \times 10^7$ cm s^{-1} [30]); second, it exhibits an ultrasmall, tunable Drude mass $m^* \equiv E_F / v_F^2$ (e.g., at $E_F = 0.2$ eV, $m^*/m_e \approx 4\%$), allowing ultrahigh cyclotron frequencies $\omega_c \equiv eB/cm^* = eBv_F^2/cE_F$ up to the terahertz range [32–34]; and third, high-quality graphene can exhibit exceptionally long intrinsic relaxation times $1/\gamma$, extending into the picosecond range [35,36]. These properties enable topological plasmons of unprecedentedly high frequency, short wavelength, long propagation, and large topological band gaps.

The plasmonic properties of a general graphene domain $\mathbf{r} \in \Omega \subseteq \mathbb{R}^2$ under an external magnetic field $\mathbf{B} = B\hat{\mathbf{z}}$ is described by a linear eigenvalue problem with three field components: the scalar potential Φ and the surface electric current density $\mathbf{J} \equiv \mathrm{J}_x \hat{\mathbf{x}} + \mathrm{J}_y \hat{\mathbf{y}}$ [18]. For an eigenstate indexed by ν and frequency ω_ν, this eigenproblem is specified by [37]

$$\hat{\mathcal{H}} \mathbf{U}_\nu = \omega_\nu \mathbf{U}_\nu, \tag{1a}$$

$$\text{with } \mathbf{U}_\nu \equiv \begin{pmatrix} \omega_F \Phi \\ \mathbf{J} \end{pmatrix} \text{ and } \hat{\mathcal{H}} \equiv \begin{pmatrix} 0 & \omega_F \hat{V} \hat{\mathbf{p}}^T \\ \alpha \hat{\mathbf{p}} & \omega_c \sigma_2 \end{pmatrix}. \tag{1b}$$

Here, $\hat{\mathbf{p}} \equiv -i\boldsymbol{\nabla}$ is the in-plane momentum operator, $\hat{V}[f](\mathbf{r}) \equiv \int_\Omega f(\mathbf{r}')/|\mathbf{r} - \mathbf{r}'| \, d^2\mathbf{r}'$ the Coulomb operator, $\sigma_2 \equiv \left(\begin{smallmatrix} 0 & -i \\ i & 0 \end{smallmatrix}\right)$ a Pauli matrix, $\omega_F \equiv E_F/\hbar$ the Fermi "frequency," and $\alpha \equiv e^2/\pi\hbar$ a prefactor of graphene's intraband conductivity $i\alpha\omega_F\omega^{-1}$. Conceptually, Eqs. (1) comprise the Coulomb, continuity, and constitutive equations. The no-spill boundary condition $\mathbf{J} \cdot \hat{\mathbf{n}} = 0$ applies along the perimeter of Ω (edge normal, $\hat{\mathbf{n}}$). Under a suitable inner product Eq. (1a) is Hermitian (see Supplemental Material [38]).

We explore the band topology of 2D plasmons in periodically structured graphene under magnetic-field induced $\mathcal{T}$ breaking. Figure 1(a) illustrates our design: a triangular antidot lattice of periodicity a and antidot diameter d is etched into a suspended sheet of graphene. The domain Ω in Eqs. (1) is then the torus defined by the rhombic unit cell of Fig. 2(a). Band folding splits the eigenindex ν into a band index $n = 1, 2, \ldots$ and a crystal wave vector $\mathbf{k}$ restricted to the hexagonal Brillouin zone (BZ) of Fig. 2(b). Accordingly, the eigenvectors assume the Bloch form $\mathbf{U}_{n\mathbf{k}}(\mathbf{r}) = \mathbf{u}_{n\mathbf{k}}(\mathbf{r}) e^{i\mathbf{k}\cdot\mathbf{r}}$, with periodic component $\mathbf{u}_{n\mathbf{k}} \equiv (\omega_F \phi, \mathbf{j})^T_{n\mathbf{k}}$.

First, we consider the simple but instructive $d = 0$ scenario, i.e., the uniform sheet, see Fig. 1(b). This "empty lattice" captures the essential impact of band folding: by folding the uniform sheet plasmon dispersion, $\omega(k) = \sqrt{2\pi\alpha\omega_F k + \omega_c^2}$, over the hexagonal BZ, threefold Dirac-like point degeneracies arise between the $n = 1, 2$, and 3 bands at the $\mathbf{K}$ (and $\mathbf{K}'$) point. For $B = 0$, the lattice's C_{6v} symmetry guarantees that twofold-degenerate Dirac points remain between the $n = 1$ and 2 bands even when $d \neq 0$. The uniform-sheet Dirac point plasmon frequency, $\omega_\mathbf{K} \equiv \sqrt{(\omega_\mathbf{K}^0)^2 + \omega_c^2}$ with $\omega_\mathbf{K}^0 \equiv \sqrt{2\pi\alpha\omega_F |\mathbf{K}|}$ and $|\mathbf{K}| = 4\pi/3a$, along with the cyclotron frequency ω_c, then define the

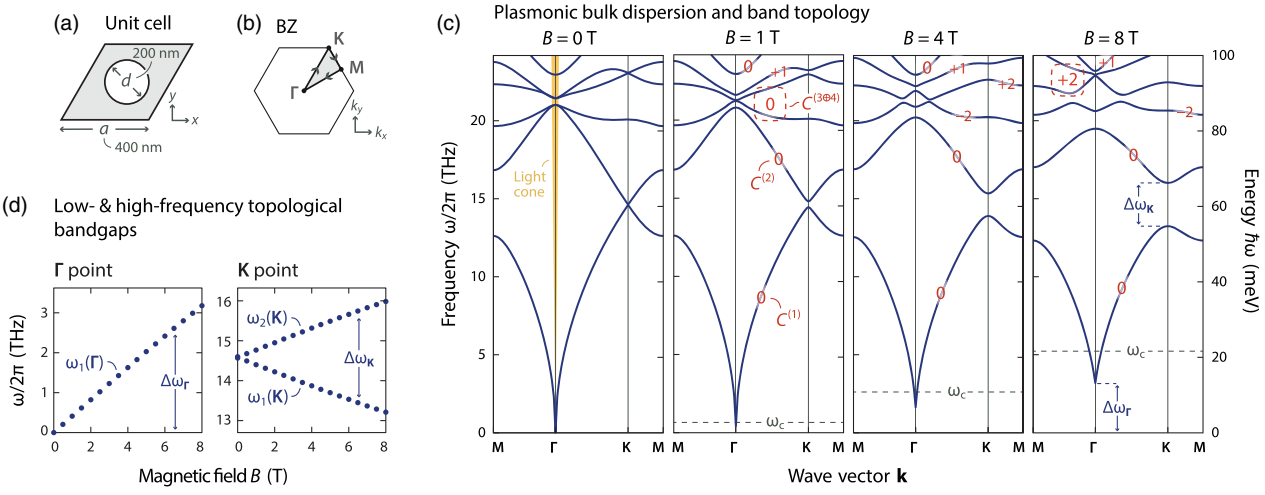

FIG. 2. Bulk properties. (a) Unit cell. (b) Brillouin zone. (c) Bulk dispersion along the high-symmetry directions of the irreducible BZ for $B = 0$, 1, 4, and 8 T. Chern numbers are indicated in orange labels; composite Chern numbers are highlighted by a dashed periphery. (d) Splitting of $\mathbf{\Gamma}$ and $\mathbf{K}$ point degeneracies and opening of low- and high-frequency topological band gaps with increasing magnetic field.

characteristic frequencies of the problem and are indicated in Fig. 1(b). By applying a finite B field to the $d \neq 0$ system, the Dirac point degeneracy is split, inducing a gap linearly proportional to ω_c. As a result, topological plasmons with both high frequency and sufficient topological gap require simultaneously large $\omega_{\mathbf{K}}^0$ and ω_c.

The parameter space involved in simultaneously maximizing $\omega_{\mathbf{K}}^0$ and ω_c is illustrated in Fig. 1(c). The monotonic E_F-dependence of the two characteristic frequencies is opposite, highlighting an inherent trade-off between the operating frequency and the gap size. In addition, the accessible parameter space is restricted by several constraints, indicated by gray regions in Fig. 1(c): first, intrinsic Drude loss estimated at $\gamma/2\pi \sim 1$ THz smears out the gap region, necessitating $\omega_c \gtrsim \gamma$; second, interband dispersion is non-negligible when $\omega_{\mathbf{K}} \gtrsim \omega_F$ [52,53], eventually introducing significant loss through Landau damping; and third, Landau quantization of the charge carriers ultimately invalidates a semiclassical description [54,55] when $E_F \lesssim E_L \equiv v_F\sqrt{2\hbar eB/c}$ (the first Landau level), or equivalently, when $\hbar\omega_c \lesssim \frac{1}{2}E_L$, see Supplemental Material [38]. Overall, we find that an experimentally favorable region exists for Fermi energies $E_F \sim 0.2$–0.3 eV, periodicities $a \sim 100$–600 nm, and magnetic fields $B \sim 2$–8 T.

Next, we turn to the nanostructured system, settling on a periodicity $a = 400$ nm, antidot diameter $d = 200$ nm, see Fig. 2(a), and a Fermi level $E_F = 0.2$ eV (equivalent, at $B = 0$, to a carrier density $n \approx 3 \times 10^{12}$ cm^{-2}). Antidot lattices like these are well within experimental capabilities [56–60]. The eigenvalue problem, Eqs. (1), is solved numerically by discretizing in an unstructured triangular mesh, employing linear nodal functions, and with the lattice-specific Coulomb interaction evaluated by Ewald summation (see Supplemental Material [38]). Figure 2(c) depicts the calculated plasmon dispersion $\omega_n(\mathbf{k})$ along the boundary of the irreducible BZ for increasing magnetic field strength $B = 0, 1, 4$, and 8 T.

In the nonmagnetic scenario, $B = 0$, the lattice disperses like the uniform sheet under the substitution $k \to \zeta_n(\mathbf{k})/a$, i.e., as $\omega_n^0(\mathbf{k}) = \sqrt{2\pi\alpha\omega_F\zeta(\mathbf{k})/a}$, with modal parameter $\zeta_n(\mathbf{k})$ solely dependent on a/d and the *relative* location of $\mathbf{k}$ in the BZ [61]; e.g., at $a/d = 2$ we find $\zeta_{1,2}(\mathbf{K}) \approx 2.535$. Near the Γ point $\zeta_1(\mathbf{k}) \propto |\mathbf{k}|$, yielding the conventional long-wavelength 2D plasmon dispersion $\omega \propto \sqrt{k}$. Particle-hole symmetry ($\mathcal{C}$) of Eqs. (1) entails the existence of a corresponding set $\{n = -1, -2, \ldots\}$ of negative energy states, $\omega_{-n}(\mathbf{k}) = -\omega_n(-\mathbf{k})$ (and a zero-frequency band, $n = 0$) [18]: accordingly, besides the Dirac point degeneracy at $\mathbf{K}$ between the $n = 1$ and 2 bands, an implicit degeneracy exists at $\mathbf{\Gamma}$ between the $n = \pm 1$ (and $n = 0$) bands. By applying a magnetic field, the bands are linearly perturbed from $\omega_n^0(\mathbf{k})$ to $\omega_n(\mathbf{k}) \simeq \omega_n^0(\mathbf{k}) + \xi_n(\mathbf{k})\omega_c + \mathcal{O}(\omega_c^2)$ (see Supplemental Material [38]); the modal perturbation parameter $\xi_n(\mathbf{k})$ is obtained numerically at the degeneracy points as $\xi_1(\mathbf{\Gamma}) \approx 0.63$ and $\xi_{1,2}(\mathbf{K}) \approx \mp 0.27$ at $a/d = 2$ [62]. This is illustrated in Fig. 2(d): the degeneracies at $\mathbf{\Gamma}$ and $\mathbf{K}$ are linearly and evenly gapped when $B \neq 0$. As we explain shortly, the low-frequency gap opened at $\mathbf{\Gamma}$ supports a topological edge state entirely analogous to its uniform sheet counterpart. The high-frequency ($\approx$15 THz) gap opening at $\mathbf{K}$, however, introduces a new, qualitatively distinct topological edge state.

Next, we describe the topological properties of the plasmonic lattice as quantified by the band Chern number, $C^{(n)} \equiv (2\pi i)^{-1}\oint_{\partial\mathrm{BZ}}\langle \mathbf{u}_{n\mathbf{k}}|\nabla_{\mathbf{k}}|\mathbf{u}_{n\mathbf{k}}\rangle\, d\mathbf{k}$ (evaluated numerically from the computed eigenvectors [64]). Figure 2(b) depicts the evolution of $C^{(n)}$ across $B = 0, 1, 4$, and 8 T. At $B = 0$ T, the Berry flux is identically zero, cf. time-reversal and parity symmetry; the band structure is topologically trivial. For $B \neq 0$, $\mathcal{T}$ is broken, allowing nonzero Berry flux and nontrivial topology: the first and second bands are gapped for all B and have $C^{(1)} = C^{(2)} = 0$. Conversely, the higher order bands, $n = 3, 4, \ldots$, display Chern numbers covering a broader range, up to ± 2. A few bands exhibit point degeneracies within numerical accuracy and are assigned a composite Chern number $C^{(n\oplus n+1)}$. As the B field is increased, there is an exchange of Chern numbers between the $n = 4, 5$, and 6 bands as gaps close and reopen, illustrating the mechanism of Berry flux monopole exchange. For even stronger B fields (see Supplemental Material [38]), all six bands eventually separate completely, leaving $C^{(1)} = C^{(2)} = 0$, $C^{(3)} = -2$, and $C^{(4)} = C^{(5)} = C^{(6)} = +1$.

By the bulk-edge correspondence, the existence of topologically protected edge states is intimately linked with the bulk topology, i.e., with $C^{(n)}$. As recently pointed out in Ref. [18], the presence of $\mathcal{C}$ symmetry, and the concomitant existence of a set of negative-frequency states $\{n = -1, -2, \ldots\}$, necessitates a global perspective of the band topology for the definition of associated gap Chern numbers. Specifically, the total Chern number of positive ($+$) and negative ($-$) frequency bands is $C_\pm \equiv \sum_{n=1}^{\infty} C^{(\pm n)}$. In uniform graphene $C_\pm = \pm\mathrm{sgn}\, B$ [18]. Since Chern numbers can be annihilated or created (pairwise) only under band closings, this result holds in nanostructured graphene as well; cf. the finite band gap separating positive and negative bands. With this in mind, we define the nth gap Chern number $\bar{C}_n$ associated with the gap immediately below the nth band as

$$\bar{C}^{(n)} \equiv \sum_{n'=-\infty}^{n-1} C^{(n')} = -\mathrm{sgn}\, B + \sum_{n'=1}^{n-1} C^{(n')}, \qquad (2)$$

specializing to positive-frequency gaps at the last equality. For lattice terminations adjacent to vacuum, bulk-edge correspondence then requires that the number of left minus right propagating topological edge states equal $\bar{C}^{(n)}$ [65].

These considerations predict the existence of single-mode one-way edge states in the first and second gaps when $B \neq 0$ and multimode one-way edge states in the

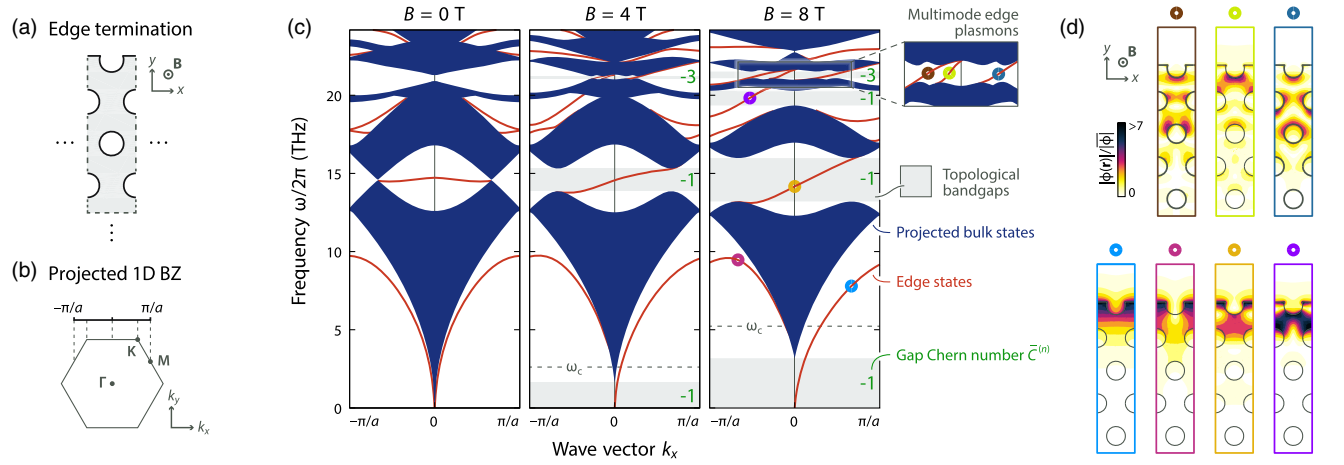

FIG. 3. Plasmonic one-way edge states at lattice terminations. (a) Edge termination of the 2D crystal. (b) Projected 1D BZ and its high symmetry points. (c) Projected bulk bands (blue) and topologically protected one-way plasmonic edge states (red) along k_x for $B = 0, 4$, and 8 T, with associated gap Chern numbers $\bar{C}^{(n)}$ (green). (d) Typical mode profiles of edge states in real space at $B = 8$ T; band association is indicated by colored markers in (c).

gap between the $n = 3$, and 4 bands at $B = 4$ and 8 T, cf. Fig. 2(c). We confirm these predictions in Fig. 3 by numerically calculating the edge states supported by a broad ribbon (20 unit cells wide) extended along x with the particular edge termination of Fig. 3(a). The bulk states are folded into the projected 1D BZ, $k_x \in (-\pi/a, \pi/a)$, see Fig. 3(b), due to breaking of Bloch periodicity along y. Additionally, edge states emerge: they are identified and postselected from the ribbon spectrum by their edge confinement and bulk-gap habitation (in emulating single-boundary physics, edge states localized on the bottom ribbon edge are omitted). The resulting edge dispersion is shown in Fig. 3(c) for $B = 0$, 4 and 8 T. At $B = 0$, all edge states are nontopological; states at $\pm\mathbf{k}$ travel in opposite directions and edge connections between bulk bands are trivial. For $B \neq 0$, topological one-way edge states appear in the band gaps, consistent with the obtained gap Chern numbers. They connect upper and lower bulk bands, occasionally by circling the 1D BZ, separated by nontrivial $\bar{C}^{(n)} \neq 0$ gaps. The edge states propagate to the right, consistent with the sign (chirality) of $\bar{C}^{(n)} \neq 0$. They are topologically protected from backscattering only in the complete band gap: above it, any defect may scatter them to either bulk or counterpropagating edge states. The low-frequency $\bar{C}^{(1)} = -1$ gap hosts edge states entirely analogous to the edge magnetoplasmons of the uniform sheet—an edge-state parallel of the bulk dispersion-agreement ($\propto \sqrt{k}$) between the $n = 1$ band and the uniform sheet. In contrast, the high-frequency (≈15 THz) edge state in the $\bar{C}^{(2)} = -1$ gap results directly from band engineering, and is a qualitatively new type of edge magnetoplasmon. Finally, a multimode triple of edge states appears in the $\bar{C}^{(4)} = -3$ gap. Though the gap is comparatively small, it can be widened by tuning a/d. Figure 3(d) illustrates the sharp spatial Bloch mode confinement of the edge states, $|\phi_{nk_x}(\mathbf{r})|$, for a few select n and k_x at $B = 8$ T. The degree of confinement correlates positively with the size of the topological band gap, i.e., implicitly with B, paralleling the uniform 2D electron gas [20].

The edge states can be efficiently excited by nearby point sources, as demonstrated in Fig. 4: a y-polarized dipole near the edge, emitting in the gap center (14.6 THz) of the $n = 1$ and 2 bands, excites the edge plasmon at $k_x = 0$ (for computational details, see Supplemental Material [38]). In the absence of intrinsic material loss, the edge state propagates unidirectionally to the right with constant amplitude as seen in Figs. 4(b)–4(d). Topological protection ensures that even structural defects, such as the sharp trench in Fig. 4(d), are traversed without backscattering. The increased edge confinement with mounting magnetic field is exemplified by Figs. 4(b)–4(c).

The edge state's topological nature does not shield it from intrinsic material or radiation loss. While the latter is negligible, owing to the strongly confined and electrostatic nature of graphene plasmons [cf. the nearly vertical light cone in Fig. 2(c)], the former can be appreciable, as in all plasmonic systems. Finite relaxation γ is readily incorporated in Eqs. (1) by the substitution $\omega_\nu \to \omega_\nu + i\gamma$. This introduces an imaginary spectral component, $\mathrm{Im}\,\omega_\nu \simeq -\frac{1}{2}\gamma(1 + \xi_\nu \omega_c/\mathrm{Re}\,\omega_\nu^0)$ for $\gamma \ll \mathrm{Re}\,\omega_\nu^0$. This impacts the propagation of edge states in two aspects: first, it blurs the gap region, allowing small but finite loss-induced coupling between edge and bulk states (see Supplemental Material [38]); second, states exhibit a finite lifetime, or, equivalently, finite propagation length $\propto 1/\gamma$, as illustrated in Fig 4(e). Strategies to reduce the relative impact of intrinsic loss include reducing the lattice constant a, increasing E_F, or maximizing the edge state group velocity by structural design (see Supplemental Material [38]).

In conclusion, we have demonstrated the band topology of 2D plasmons in periodically patterned graphene under a $\mathcal{T}$-breaking magnetic field. Multiple sets of topologically

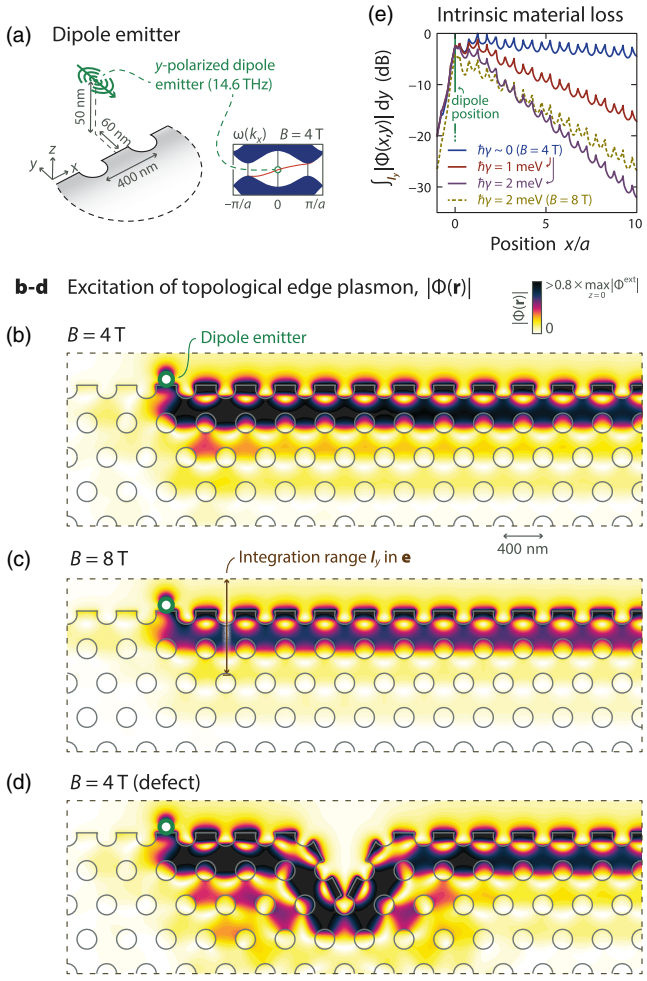

FIG. 4. Dipole excitation of edge plasmons in the $\bar{C}^{(2)} = -1$ gap. (a) Dipole configuration relative to nanostructured graphene edge. (b)–(d) Total potential $|\Phi(\mathbf{r})|$ of dipole-excited one-way edge plasmons for $\gamma \sim 0$ (implemented as $\hbar\gamma = 0.15$ meV for computational reasons, see Supplemental Material [38]) at (b) $B = 4$ T, (c) $B = 8$ T, and (d) $B = 4$ T with a structural defect. (e) Attenuated forward propagation due to intrinsic material loss, illustrated by the y-integrated absolute potential.

protected one-way edge plasmons corresponding to nontrivial gap Chern numbers are discovered. Their operating frequencies can be as high as tens of terahertz, i.e., in the far-infrared regime. They can be experimentally verified by terahertz near-field imaging [66,67] and Fourier transform infrared spectroscopy [60]. Our findings suggests a new direction in the synthesis of high-frequency $\mathcal{T}$ broken topological bosonic phases, and can be directly extended to nonmagnetic schemes based on valley polarization [68,69].

D. J., N. X. F., and X. Z. acknowledge financial support by the NSF (Grant No. CMMI-1120724) and AFOSR MURI (Award No. FA9550-12-1-0488). T. C. acknowledges financial support from Villum Fonden and the Danish Council for Independent Research (Grant No. DFF–6108-00667). M. S. was supported in part by the Army Research Office through the Institute for Soldier Nanotechnologies (Contract No. W911NF-13-D-0001). L. L. was supported in part by the National Key Research and Development Program of China (Grants No. 2017YFA0303800 and No. 2016YFA0302400) and in part by the National Thousand-Young-Talents Program of China.

D. J. and T. C. contributed equally to this work.

*dafeijin@berkeley.edu
†tchr@mit.edu
‡linglu@iphy.ac.cn
§xzhang@me.berkeley.edu

[1] K. v. Klitzing, G. Dorda, and M. Pepper, Phys. Rev. Lett. **45**, 494 (1980).
[2] F. D. M. Haldane, Phys. Rev. Lett. **61**, 2015 (1988).
[3] Z. Wang, Y. Chong, J. D. Joannopoulos, and M. Soljačić, Nature (London) **461**, 772 (2009).
[4] S. A. Skirlo, L. Lu, Y. Igarashi, Q. Yan, J. Joannopoulos, and M. Soljačić, Phys. Rev. Lett. **115**, 253901 (2015).
[5] L. M. Nash, D. Kleckner, A. Read, V. Vitelli, A. M. Turner, and W. T. M. Irvine, Proc. Natl. Acad. Sci. U.S.A. **112**, 14495 (2015).
[6] F. D. M. Haldane and S. Raghu, Phys. Rev. Lett. **100**, 013904 (2008).
[7] E. Prodan and C. Prodan, Phys. Rev. Lett. **103**, 248101 (2009).
[8] P. Wang, L. Lu, and K. Bertoldi, Phys. Rev. Lett. **115**, 104302 (2015).
[9] R. Shindou, R. Matsumoto, S. Murakami, and J. I. Ohe, Phys. Rev. B **87**, 174427 (2013).
[10] J. Yuen-Zhou, S. K. Saikin, N. Y. Yao, and A. Aspuru-Guzik, Nat. Mater. **13**, 1026 (2014).
[11] T. Karzig, C.-E. Bardyn, N. H. Lindner, and G. Refael, Phys. Rev. X **5**, 031001 (2015).
[12] R. Fleury, D. L. Sounas, C. F. Sieck, M. R. Haberman, and A. Alù, Science **343**, 516 (2014).
[13] K. Fang, Z. Yu, and S. Fan, Nat. Photonics **6**, 782 (2012).
[14] M. Hafezi and P. Rabl, Opt. Express **20**, 7672 (2012).
[15] L. D. Tzuang, K. Fang, P. Nussenzveig, S. Fan, and M. Lipson, Nat. Photonics **8**, 701 (2014).
[16] Z. Shen, Y.-L. Zhang, Y. Chen, C.-L. Zou, Y.-F. Xiao, X.-B. Zou, F.-W. Sun, G.-C. Guo, and C. Dong, Nat. Photonics **10**, 657 (2016).
[17] K. Fang, J. Luo, A. Metelmann, M. H. Matheny, F. Marquardt, A. A. Clerk, and O. Painter, Nat. Phys. **13**, 465 (2017).
[18] D. Jin, L. Lu, Z. Wang, C. Fang, J. D. Joannopoulos, M. Soljačić, L. Fu, and N. X. Fang, Nat. Commun. **7**, 13486 (2016).
[19] D. B. Mast, A. J. Dahm, and A. L. Fetter, Phys. Rev. Lett. **54**, 1706 (1985).
[20] V. A. Volkov and S. A. Mikhailov, Sov. Phys. JETP **67**, 1639 (1988).
[21] The emerging branches of topological plasmonics encompass both $\mathcal{T}$-invariant [22–24] and $\mathcal{T}$-broken [25,26] systems: our focus is the plasmonic analogue of the quantum anomalous Hall effect (i.e., $\mathcal{T}$-broken and $\mathbb{Z}$ topology).

[22] L. Ge, L. Wang, M. Xiao, W. Wen, C. T. Chan, and D. Han, Opt. Express **23**, 21585 (2015).

[23] L. Wang, R.-Y. Zhang, M. Xiao, D. Han, C. T. Chan, and W. Wen, New J. Phys. **18**, 103029 (2016).

[24] H. Deng, X. Chen, N. C. Panoiu, and F. Ye, Opt. Lett. **41**, 4281 (2016).

[25] W. Gao, B. Yang, M. Lawrence, F. Fang, B. Béri, and S. Zhang, Nat. Commun. **7**, 12435 (2016).

[26] S. A. H. Gangaraj, M. G. Silveirinha, and G. W. Hanson, IEEE JMMCT **2**, 2379 (2016).

[27] D. K. Efetov and P. Kim, Phys. Rev. Lett. **105**, 256805 (2010).

[28] H. Liu, Y. Liu, and D. Zhu, J. Mater. Chem. **21**, 3335 (2011).

[29] Z. Fang, Y. Wang, A. E. Schlather, Z. Liu, P. M. Ajayan, F. J. García de Abajo, P. Nordlander, X. Zhu, and N. J. Halas, Nano Lett. **14**, 299 (2014).

[30] Consistent with a 2.8 eV nearest-neighbor hopping [31].

[31] A. H. C. Neto, F. Guinea, N. M. R. Peres, K. S. Novoselov, and A. K. Geim, Rev. Mod. Phys. **81**, 109 (2009).

[32] I. Crassee, M. Orlita, M. Potemski, A. L. Walter, M. Ostler, T. Seyller, I. Gaponenko, J. Chen, and A. Kuzmenko, Nano Lett. **12**, 2470 (2012).

[33] H. Yan, Z. Li, X. Li, W. Zhu, P. Avouris, and F. Xia, Nano Lett. **12**, 3766 (2012).

[34] I. Petković, F. I. B. Williams, K. Bennaceur, F. Portier, P. Roche, and D. C. Glattli, Phys. Rev. Lett. **110**, 016801 (2013).

[35] X. Du, I. Skachko, A. Barker, and E. Y. Andrei, Nat. Nanotechnol. **3**, 491 (2008).

[36] K. I. Bolotin, K. J. Sikes, Z. Jiang, M. Klima, G. Fudenberg, J. Hone, P. Kim, and H. L. Stormer, Solid State Commun. **146**, 351 (2008).

[37] A nonretarded, intraband approach is adopted; this neglects coupling of plasmons to free-space photons and interband dispersion, justified, respectively, by the large mismatch between photon and plasmon wave vectors and the restriction to frequencies small relative to the interband threshold at $2E_F$.

[38] See Supplemental Material at http://link.aps.org/supplemental/10.1103/PhysRevLett.118.245301 for additional details, derivations, and results, which includes Refs. [39–51]

[39] W. Wang, T. Christensen, A.-P. Jauho, K. S. Thygesen, M. Wubs, and N. A. Mortensen, Sci. Rep. **5**, 9535 (2015).

[40] I. Gohberg, P. Lancaster, and L. Rodman, *Matrix Polynomials* (SIAM, Philadelphia, 2009).

[41] P. Lancaster, I. N. Sneddon, M. Stark, and J. P. Kahane, *Lambda-matrices and Vibrating Systems*, 1st ed. (Pergamon Press, New York, 1966).

[42] J. E. Pask, B. M. Klein, P. A. Sterne, and C. Y. Fong, Comput. Phys. Commun. **135**, 1 (2001).

[43] D. R. Wilton, S. M. Rao, A. W. Glisson, D. H. Schaubert, O. M. Al-Bundak, and C. M. Butler, IEEE Trans. Antennas Propag. **32**, 276 (1984).

[44] J. M. Ziman, *Principles of the Theory of Solids*, 2nd ed. (Cambridge University Press, Cambridge, England, 1972).

[45] B. Gallinet, A. M. Kern, and O. J. F. Martin, J. Opt. Soc. Am. A **27**, 2261 (2010).

[46] D. Sun, J. Manges, X. Yuan, and Z. Cendes, IEEE Trans. Antennas Propag. **37**, 12 (1995).

[47] S. M. Rao, D. R. Wilton, and A. W. Glisson, IEEE Trans. Antennas Propag. **30**, 409 (1982).

[48] K. D. Ikramov, J. Comput. Math. Sci. Teach. **64**, 783 (1993).

[49] I. S. Gradshteyn and I. M. Ryzhik, *Table of Integrals, Series, and Products*, 7th ed. (Academic Press, New York, 2007).

[50] O. L. Berman, G. Gumbs, and Y. E. Lozovik, Phys. Rev. B **78**, 085401 (2008).

[51] R. Roldán, J.-N. Fuchs, and M. O. Goerbig, Phys. Rev. B **80**, 085408 (2009).

[52] B. Wunsch, T. Stauber, F. Sols, and F. Guinea, New J. Phys. **8**, 318 (2006).

[53] E. H. Hwang and S. Das Sarma, Phys. Rev. B **75**, 205418 (2007).

[54] V. P. Gusynin, S. G. Sharapov, and J. P. Carbotte, J. Phys. Condens. Matter **19**, 026222 (2007).

[55] A. Ferreira, N. M. R. Peres, and A. H. C. Neto, Phys. Rev. B **85**, 205426 (2012).

[56] J. Bai, X. Zhong, S. Jiang, Y. Huang, and X. Duan, Nat. Nanotechnol. **5**, 190 (2010).

[57] B. Zhu, G. Ren, Y. Gao, Y. Yang, Y. Lian, and S. Jian, Opt. Express **22**, 24096 (2014).

[58] K. Y. M. Yeung, J. Chee, H. Yoon, Y. Song, J. King, and D. Ham, Nano Lett. **14**, 2479 (2014).

[59] P. Q. Liu, F. Valmorra, C. Maissen, and J. Faist, Optica **2**, 135 (2015).

[60] J.-M. Poumirol, P. Q. Liu, T. M. Slipchenko, A. Y. Nikitin, L. Martin-Moreno, J. Faist, and A. B. Kuzmenko, Nat. Commun. **8**, 14626 (2017).

[61] T. Christensen, *From Classical to Quantum Plasmonics in Three and Two Dimensions* (Springer Theses, New York, 2017).

[62] In the uniform sheet ($d = 0$) the shift at Γ is exactly ω_c [63], corresponding to $\xi_1(\Gamma) = 1$; finite antidots ($d \neq 0$) lower the effective electron density instating a monotonic reduction of $\xi_1(\Gamma)$ with increasing d/a.

[63] T. Ando, A. B. Fowler, and F. Stern, Rev. Mod. Phys. **54**, 437 (1982).

[64] T. Fukui, Y. Hatsugai, and H. Suzuki, J. Phys. Soc. Jpn. **74**, 1674 (2005).

[65] Y. Hatsugai, Phys. Rev. Lett. **71**, 3697 (1993).

[66] J. Chen, M. Badioli, P. Alonso-González, S. Thongrattanasiri, F. Huth, J. Osmond, M. Spasenović, A. Centeno, A. Pesquera, P. Godignon, A. Z. Elorza, N. Camara, F. J. García de Abajo, R. Hillenbrand, and F. H. L. Koppens, Nature (London) **487**, 77 (2012).

[67] Z. Fei, A. S. Rodin, G. O. Andreev, W. Bao, A. S. McLeod, M. Wagner, L. M. Zhang, Z. Zhao, M. Thiemens, G. Dominguez, M. M. Fogler, A. H. C. Neto, C. N. Lau, F. Keilmann, and D. N. Basov, Nature (London) **487**, 82 (2012).

[68] A. Kumar, A. Nemilentsau, K. H. Fung, G. Hanson, N. X. Fang, and T. Low, Phys. Rev. B **93**, 041413 (2016).

[69] J. C. W. Song and M. S. Rudner, Proc. Natl. Acad. Sci. U.S.A. **113**, 4658 (2016).

SUPPLEMENTAL MATERIAL

Infrared Topological Plasmons in Graphene

Dafei Jin,[1,*] Thomas Christensen,[2,*] Marin Soljačić,[2] Nicholas X. Fang,[3] Ling Lu,[4,†] and Xiang Zhang[1,‡]

[1] *Department of Mechanical Engineering, University of California, Berkeley, California 94720, USA*
[2] *Department of Physics, Massachusetts Institute of Technology, Cambridge, Massachusetts 02139, USA*
[3] *Department of Mechanical Engineering, Massachusetts Institute of Technology, Cambridge, Massachusetts 02139, USA*
[4] *Institute of Physics, Chinese Academy of Sciences/Beijing National Laboratory for Condensed Matter Physics, Beijing 100190, China*

I. NUMERICAL METHOD

We here outline the essential features of the numerical method employed in the Letter and implemented in an in-house code. The method is a generalization of that discussed in Ref. S1, extended to treat anisotropic response and 1D and 2D periodicity. We also discuss certain technical aspects of the calculations in Fig. 4.

A. Formulation of a scalar eigenvalue problem

We first briefly describe how the problem considered in Eqs. (1) of the main text, can be recast as a scalar eigenvalue problem, suitable for numerical discretization. The continuity, constitutive and Coulomb equations form the ingredients of Eqs. (1); expressed in terms of the potential Φ and surface charge density ρ they read (frequency-dependence of field quantities suppressed):

$$\rho(\mathbf{r}) = \frac{1}{\mathrm{i}\omega}\nabla\cdot\mathbf{J}(\mathbf{r}) = \frac{-1}{\mathrm{i}\omega}\nabla\cdot[\boldsymbol{\sigma}(\omega)\nabla\Phi(\mathbf{r})], \qquad \Phi(\mathbf{r}) = \Phi^{\mathrm{ext}}(\mathbf{r}) + \int_\Omega \frac{\rho(\mathbf{r}')}{|\mathbf{r}-\mathbf{r}'|}\,\mathrm{d}^2\mathbf{r}'. \tag{S1}$$

with coordinates and nabla operators restricted to a two-dimensional domain $\Omega \subseteq \mathbb{R}^2$. Here, $\boldsymbol{\sigma}(\omega) \equiv \left(\begin{smallmatrix}\sigma_{xx} & \sigma_{xy}\\ -\sigma_{xy} & \sigma_{xx}\end{smallmatrix}\right)(\omega)$ denotes a general anisotropic surface conductivity. The equations can be nondimensionalized by switching to dimensionless variables $\mathbf{r} \to L\mathbf{r}$, $\nabla \to L^{-1}\nabla$, and $\Omega \to L\Omega$ normalized by a characteristic length L of the domain (this nondimensionalization is implicitly adopted *throughout* Section I):

$$\rho(\mathbf{r}) = \frac{-1}{\mathrm{i}\omega L^2}\nabla\cdot[\boldsymbol{\sigma}(\omega)\nabla\Phi(\mathbf{r})], \qquad \Phi(\mathbf{r}) = \Phi^{\mathrm{ext}}(\mathbf{r}) + L\int_\Omega \frac{\rho(\mathbf{r}')}{|\mathbf{r}-\mathbf{r}'|}\,\mathrm{d}^2\mathbf{r}'. \tag{S2}$$

For the sake of brevity and clarity, these equations are recast in operator form as

$$|\rho\rangle = \frac{-1}{\mathrm{i}\omega L^2}[\sigma_{xx}(\omega)\mathsf{D}^{\mathsf{i}} + \sigma_{xy}(\omega)\mathsf{D}^{\mathsf{a}}]|\Phi\rangle, \qquad |\Phi\rangle = |\Phi^{\mathrm{ext}}\rangle + L\mathsf{V}|\rho\rangle, \tag{S3}$$

with operators D^{i} and D^{a} representing the isotropic and anisotropic[1] contributions to the continuity equation and V the Coulomb interaction, such that:[2]

$$\langle\mathbf{r}|\mathsf{D}^{\mathsf{i}}|\Phi\rangle \equiv \nabla\cdot[\nabla\Phi(\mathbf{r})], \qquad \langle\mathbf{r}|\mathsf{D}^{\mathsf{a}}|\Phi\rangle \equiv \nabla\cdot[\left(\begin{smallmatrix}0 & 1\\ -1 & 0\end{smallmatrix}\right)\nabla\Phi(\mathbf{r})], \qquad \langle\mathbf{r}|\mathsf{V}|\rho\rangle \equiv \int_\Omega \frac{\rho(\mathbf{r}')}{|\mathbf{r}-\mathbf{r}'|}\,\mathrm{d}^2\mathbf{r}'. \tag{S4}$$

In the absence of anisotropy, $\sigma_{xy} = 0$, and external potentials, $\Phi^{\mathrm{ext}} = 0$, these equations produce a simple *linear* eigenproblem $\zeta_\nu|\rho_\nu\rangle = -(2\pi)^{-1}\mathsf{D}^{\mathsf{i}}\mathsf{V}|\rho_\nu\rangle$ with frequency- and scale-dependent eigenvalues $\zeta_\nu \equiv \mathrm{i}\omega_\nu L/2\pi\sigma_{xx}(\omega_\nu)$ [S2]. In contrast, for a general nonzero anisotropy the governing equations yield

---

[1] The operator D^{a} is evidently equal to the commutator $[\partial_x, \partial_y]\Phi(\mathbf{r})$; we emphasize that this commutator is nonzero only when a boundary $\partial\Omega$ delimits the domain Ω (i.e. not when $\Omega = \mathbb{R}^2$), in which case a boundary condition on $\mathbf{J}$ breaks commutativity.

[2] Sub- or superstrates of dielectric function $\varepsilon_\pm$ can be incorporated by rescaling the Coulomb interaction $\mathsf{V} \to 2(\varepsilon_- + \varepsilon_+)^{-1}\mathsf{V}$.

a *nonlinear* matrix equation $\mathrm{i}\omega_\nu L|\rho_\nu\rangle = -\sigma_{xx}(\omega_\nu)\mathsf{D}^{\mathsf{i}}\mathsf{V}|\rho_\nu\rangle - \sigma_{xy}(\omega_\nu)\mathsf{D}^{\mathsf{a}}\mathsf{V}|\rho_\nu\rangle$ in the eigenfrequency ω_ν. Fortunately, for the semiclassical intraband description of graphene's magnetoconductivity,[3] this general matrix equation reduces to a cubic eigenvalue problem, reading—for $\gamma = 0$, it reads:[4]

$$\Big[\lambda_\nu^3 \mathsf{1} - \lambda_\nu\Big(\mathsf{1} - \tfrac{1}{2\pi\zeta_\mathrm{c}}\mathsf{D}^{\mathsf{i}}\mathsf{V}\Big) - \tfrac{\mathrm{i}}{2\pi\zeta_\mathrm{c}}\mathsf{D}^{\mathsf{a}}\mathsf{V}\Big]|\rho_\nu\rangle = 0, \tag{S5}$$

with eigenvalues $\lambda_\nu \equiv \omega_\nu/\omega_\mathrm{c}$ and setup-dependent scalar $\zeta_\mathrm{c} \equiv \mathrm{i}\omega_\mathrm{c}L/2\pi\sigma_{xx}(\omega_\mathrm{c}) = \hbar^2\omega_\mathrm{c}^2 L/2e^2E_\mathrm{F}$.

This polynomial eigenvalue problem can be rewritten as a linear eigenvalue problem by enlarging the problem's dimensionality. Specifically, a general mth order polynomial eigenvalue problem $\sum_{m'=0}^{m}\lambda^{m'}\mathsf{A}_{m'}|\mathsf{x}\rangle = 0$ spanned by operators $\mathsf{A}_{m'}$ with $N\times N$ representations has an equivalent linearized $mN\times mN$ representation. This representation follows by introducing $m' = 1,\ldots,m-1$ auxiliary unknowns $|\mathsf{x}^{(m'+1)}\rangle \equiv \lambda|\mathsf{x}^{(m')}\rangle = \lambda_\nu^{m'}|\mathsf{x}\rangle$ with $|\mathsf{x}^{(1)}\rangle \equiv |\mathsf{x}\rangle$ [S5; S6]. The cubic eigenvalue problem in Eq. (S5) is particularly simple, having the monic form $(\lambda^3 + \lambda\mathsf{A}_1 + \mathsf{A}_0)|\mathsf{x}\rangle = 0$; its linearized representation is $\tilde{\mathbf{A}}|\tilde{\mathbf{x}}\rangle = \lambda|\tilde{\mathbf{x}}\rangle$, with $\tilde{\mathbf{A}} \equiv \left(\begin{smallmatrix} 0 & 1 & 0 \\ 0 & 0 & 1 \\ -\mathsf{A}_0 & -\mathsf{A}_1 & 0 \end{smallmatrix}\right)$ with $|\tilde{\mathbf{x}}\rangle \equiv (|\mathsf{x}^{(1)}\rangle, |\mathsf{x}^{(2)}\rangle, |\mathsf{x}^{(3)}\rangle)^T$. The price paid for this linearization is a three-fold increase in representation dimensionality; for a discretized representation of Eq. (S5) this translates to a 3^3-fold increase in computational complexity compared to the isotropic (i.e. $B = 0$) eigenvalue problem.

B. Discretization in an unstructured triangular mesh

In our computational implementation, we discretize the operators in Eq. (S4) on an unstructured triangular mesh by expanding field quantities ρ and Φ in linear elements. Specifically, the domain Ω is decomposed into $j \in 1,\ldots,J$ triangular elements Ω_j such that $\Omega = \bigoplus_j \Omega_j$; the elements are specified by connections among $k = 1,\ldots,K$ vertex points $\mathbf{r}_k \in \Omega$; and field quantities are linearly interpolated from their associated vertex values. The operators' discretization then follow the usual finite-element scheme, as described in Ref. S1. Here, we focus on the aspects which are unique to the current problem, namely the specification of the weak form of $\mathsf{D}^{\mathsf{i,a}}$ and the evaluation of elements of the kernel V.

1. Continuity equation, $\mathsf{D}^{\mathsf{i,a}}$

To evaluate the operators $\mathsf{D}^{\mathsf{i,a}}$ consistent with the boundary condition $\hat{\mathbf{n}}\cdot\mathbf{J}(\mathbf{r}\in\partial\Omega) = 0$ (edge normal, $\hat{\mathbf{n}}$), Eq. (S2) is reduced to its weak form by the usual scheme; specifically, multiplying the continuity equation by a test function $v(\mathbf{r})^*$ and integrating over Ω, one finds:

$$\begin{aligned}\int_\Omega v(\mathbf{r})^*\rho(\mathbf{r})\,\mathrm{d}^2\mathbf{r} &= -\frac{1}{\mathrm{i}\omega L^2}\int_\Omega v(\mathbf{r})^*\nabla\cdot\mathbf{J}(\mathbf{r})\,\mathrm{d}^2\mathbf{r} = -\frac{1}{\mathrm{i}\omega L^2}\bigg[\oint_{\partial\Omega} v(\mathbf{r})^*\underbrace{\hat{\mathbf{n}}\cdot\mathbf{J}(\mathbf{r})}_{=0}\,\mathrm{d}\mathbf{r} - \int_\Omega \nabla v(\mathbf{r})^*\cdot\mathbf{J}(\mathbf{r})\,\mathrm{d}^2\mathbf{r}\bigg] \\ &= \frac{1}{\mathrm{i}\omega L^2}\bigg[\sigma_{xx}(\omega)\int_\Omega \nabla v(\mathbf{r})^*\cdot\nabla\Phi(\mathbf{r})\,\mathrm{d}^2\mathbf{r} + \sigma_{xy}(\omega)\int_\Omega \nabla v(\mathbf{r})^*\cdot\left(\begin{smallmatrix}0&1\\-1&0\end{smallmatrix}\right)\nabla\Phi(\mathbf{r})\,\mathrm{d}^2\mathbf{r}\bigg] \\ \Leftrightarrow\ \langle v|\mathsf{D}_\mathsf{L}|\rho\rangle &= \frac{1}{\mathrm{i}\omega L^2}\Big[\sigma_{xx}(\omega)\langle v|\mathsf{D}^{\mathsf{i}}_\mathsf{R}|\Phi\rangle + \sigma_{xy}(\omega)\langle v|\mathsf{D}^{\mathsf{a}}_\mathsf{R}|\Phi\rangle\Big].\end{aligned} \tag{S6}$$

Comparing Eq. (S3) and (S6), the operators' weak forms are identified as $\mathsf{D}^{\mathsf{i}} = -\mathsf{D}_\mathsf{L}^{-1}\mathsf{D}^{\mathsf{i}}_\mathsf{R}$ and $\mathsf{D}^{\mathsf{a}} = -\mathsf{D}_\mathsf{L}^{-1}\mathsf{D}^{\mathsf{a}}_\mathsf{R}$. Their linear element discretization is sparse, of size $K\times K$, and readily derivable in barycentric coordinates [S1].

For periodic systems, the operators retain the weak formulation of Eq. (S6) on the unit cell Ω_uc under the substitution $\nabla\to\nabla+\mathrm{i}\mathbf{k}$. The periodic boundary condition over Ω_uc poses a minor technical complication as it is of a so-called *essential* type [S7]; accordingly, it must be guaranteed at the basis level such that the meshing of Ω_uc explicitly reflects this periodicity, i.e. the mesh is a torus in 2D and a cylinder in 1D.

---

[3] The semiclassical magnetoconductivity of graphene: $\sigma_{xx}(\omega) = \frac{\mathrm{i}e^2E_\mathrm{F}}{\pi\hbar^2}\frac{\omega+\mathrm{i}\gamma}{(\omega+\mathrm{i}\gamma)^2-\omega_\mathrm{c}^2}$ and $\sigma_{xy}(\omega) = \frac{e^2E_\mathrm{F}}{\pi\hbar^2}\frac{\omega_\mathrm{c}}{(\omega+\mathrm{i}\gamma)^2-\omega_\mathrm{c}^2}$ [S3; S4].

[4] Equation (S5) generalizes to $\{\lambda_\nu^3\mathsf{1} + \lambda_\nu^2 2i\gamma_\mathrm{c}\mathsf{1} - \lambda_\nu[(1+\gamma_\mathrm{c}^2)\mathsf{1} - \frac{1}{2\pi\zeta_\mathrm{c}}\mathsf{D}^{\mathsf{i}}\mathsf{V}] - \frac{\mathrm{i}}{2\pi\zeta_\mathrm{c}}(\mathsf{D}^{\mathsf{a}} - \gamma_\mathrm{c}\mathsf{D}^{\mathsf{i}})\mathsf{V}\}|\rho_\nu\rangle = 0$ for nonzero $\gamma_\mathrm{c} \equiv \gamma/\omega_\mathrm{c}$.

2. Coulomb interaction, V

Constructing the discretized Coulomb operator (which is dense and of size $K \times K$) requires evaluation of integrals of the kind

$$V_j(\mathbf{r}) = \int_{\Omega_j} V(\mathbf{r}, \mathbf{r}')\rho(\mathbf{r}')\, \mathrm{d}^2\mathbf{r}', \tag{S7}$$

where $\mathbf{r} \in \mathbf{r}_k$ is a vertex point, $V(\mathbf{r}, \mathbf{r}')$ is the real-space form of the Coulomb interaction, and $\rho(\mathbf{r}')$ a linear, vertex-specified function[5] on Ω_j. In Ref. S1, integrals of this type were evaluated by a 16-point numerical quadrature rule.[6] However, in the absence of periodicity [i.e. when $V(\mathbf{r}, \mathbf{r}') = |\mathbf{r} - \mathbf{r}'|^{-1}$] Eq. (S7) can actually be evaluated analytically [S8], yielding improved convergence; the calculations in Fig. 4 involve tens of thousands of vertices—this analytical evaluation of Coulomb elements permits a slightly coarser mesh and a concomitant lowering of the still very appreciable memory requirements.

In the general periodic case, the real-space Coulomb interaction is periodic over the unit cell Ω_{uc} and depends explicitly on Bloch wave vector $\mathbf{k}$, taking the form of a sum over the direct lattice[7]

$$V_{\mathbf{k}}(\mathbf{r}, \mathbf{r}') = \sum_{\{\mathbf{R}\}} \frac{\mathrm{e}^{-\mathrm{i}\mathbf{k}\cdot(\mathbf{r}-\mathbf{r}'-\mathbf{R})}}{|\mathbf{r} - \mathbf{r}' - \mathbf{R}|}, \tag{S8}$$

where $\mathbf{R} = n\mathbf{R}_1 + m\mathbf{R}_2$ denotes the direct lattice vectors ($n, m \in \mathbb{Z}$). The lattice-summed Coulomb interaction is very slowly convergent, generally requiring thousands of terms (worse, it is formally divergent for $\mathbf{k} = 0$). This issue can be resolved by the techniques of Ewald summation, see e.g. Ref. S9, by *smoothly* splitting the sum into a short-range part $V^{(2)}_{\mathbf{k}}(\mathbf{r}, \mathbf{r}')$, summed in the direct lattice $\mathbf{R}$, and a long-range part $V^{(1)}_{\mathbf{k}}(\mathbf{r}, \mathbf{r}')$, summed in the reciprocal lattice $\mathbf{G}$. Here, we adopt a splitting which exploits the error function erf and its complement erfc, which allow a natural splitting since $\mathrm{erf}\, x + \mathrm{erfc}\, x = 1$. Below, we briefly outline the resulting expressions, which depend on the dimensionality of the periodicity.

Two-dimensional periodicity— The result in 2D is well-known, see e.g. Ref. S10. The result is (with $\mathbf{x} \equiv \mathbf{r} - \mathbf{r}'$ for brevity):

$$V_{\mathbf{k}}(\mathbf{x}) \equiv \underbrace{V^{(1)}_{\mathbf{k}}(\mathbf{x})}_{\text{long range}} + \underbrace{V^{(2)}_{\mathbf{k}}(\mathbf{x})}_{\text{short range}},$$

$$\text{with } V^{(1)}_{\mathbf{k}}(\mathbf{x}) \equiv \sum_{\{\mathbf{R}\}} \frac{\mathrm{e}^{-\mathrm{i}\mathbf{k}\cdot(\mathbf{x}-\mathbf{R})}}{|\mathbf{x} - \mathbf{R}|} \mathrm{erf}(|\mathbf{x} - \mathbf{R}|E) = \frac{2\pi}{|\Omega_{\mathrm{uc}}|} \sum_{\{\mathbf{G}\}} \frac{\mathrm{e}^{-\mathrm{i}\mathbf{G}\cdot\mathbf{x}}}{|\mathbf{k} - \mathbf{G}|} \mathrm{erfc}\left(\frac{|\mathbf{k} - \mathbf{G}|}{2E}\right), \tag{S9a}$$

$$\text{and } V^{(2)}_{\mathbf{k}}(\mathbf{x}) \equiv \sum_{\{\mathbf{R}\}} \frac{\mathrm{e}^{-\mathrm{i}\mathbf{k}\cdot(\mathbf{x}-\mathbf{R})}}{|\mathbf{x} - \mathbf{R}|} \mathrm{erfc}(|\mathbf{x} - \mathbf{R}|E), \tag{S9b}$$

where $|\Omega_{\mathrm{uc}}|$ denotes the unit cell area and E is the Ewald splitting parameter, chosen as $E = \sqrt{\pi/|\Omega_{\mathrm{uc}}|}$. The convergence of $V^{(1)}_{\mathbf{k}}(\mathbf{x})$ and $V^{(2)}_{\mathbf{k}}(\mathbf{x})$ is exponential in $|\mathbf{k} - \mathbf{G}|$ and $|\mathbf{x} - \mathbf{R}|$, respectively. Typically, convergence to machine precision is reached in less than ten-by-ten direct or reciprocal vectors.

Besides vastly improved convergence, the Ewald scheme has the benefit of indicating the appropriate $\mathbf{k} = 0$ limit clearly, despite its formal divergence. Concretely, if $\mathbf{k} = \boldsymbol{\delta}$ with $|\boldsymbol{\delta}| \ll 1$, the $\mathbf{G} = \mathbf{0}$ term in Eq. (S9a) diverges like $\frac{2\pi}{|\Omega_{\mathrm{uc}}|}\mathrm{e}^{-\mathrm{i}\boldsymbol{\delta}\cdot\mathbf{x}}\,\mathrm{erfc}(|\boldsymbol{\delta}|)/|\boldsymbol{\delta}| \simeq \frac{2\pi}{|\Omega_{\mathrm{uc}}|}/|\boldsymbol{\delta}|$. Crucially, this divergence is independent of $\mathbf{x}$, and, consequently does not contribute to the response, as can be proven by invoking charge conservation. Hence, for $\mathbf{k} = \mathbf{0}$, the relevant (and convergent) part of $V^{(1)}_{\mathbf{k}}(\mathbf{x})$ excludes the $\mathbf{G} = \mathbf{0}$ term [$V^{(2)}_{\mathbf{k}}(\mathbf{x})$ requires no special consideration].

---

[5] In a set of local barycentric coordinates ($\eta \in [0, 1], \xi \in [0, 1 - \eta]$) of the jth triangular element $\rho(\mathbf{r}') = \sum_{k=1}^{3} f_k(\eta, \xi)\rho_k$ where $\rho_{1,2,3}$ denotes the local vertex-values of the charge density on Ω_j.

[6] Ref. S1 erroneously indicated that a 1-point quadrature rule is sufficient to obtain a convergent method; this is not the case. In actuality, a 16-point quadrature rule was implemented and none of the results reported were affected by this misrepresentation.

[7] A numerical quadrature scheme is necessary to evaluate the mesh-integrals $V_{\mathbf{k},j}(\mathbf{r})$ of $V_{\mathbf{k}}(\mathbf{r}, \mathbf{r}')$; we adopt a 16-point scheme.

One-dimensional periodicity — The 1D Ewald sum associated with the present problem is, to the best of our knowledge, less well-known that its 2D counterpart. Regardless, its derivation follows the conventional approach. Although the long-range part is numerically less convenient than in Eqs. (S9), it can still be expressed in terms of known special functions. We consider a ribbon-geometry periodic in the primitive lattice vector $\mathbf{R}_1$. Adopting once again an (erf, erfc) splitting, the short-range term $V^{(2)}_{\mathbf{k}}(\mathbf{x})$ mirrors Eq. (S9b) (albeit restricted to a 1D lattice $\mathbf{R} = n\mathbf{R}_1$ with $n \in \mathbb{Z}$), while the long-range term reduces to a sum in the reciprocal lattice $\mathbf{G} = n\mathbf{G}_1$ (with $\mathbf{G}_1 \equiv 2\pi\mathbf{R}_1/|\mathbf{R}_1|$ in 1D):

$$V^{(1)}_{\mathbf{k}}(\mathbf{x}) = \frac{1}{|\mathbf{R}_1|}\sum_{\{\mathbf{G}\}} K_0\left(\frac{[(\mathbf{k}+\mathbf{G})\cdot\mathbf{R}_1]^2}{4E^2}, x_\perp^2 E^2\right) \mathrm{e}^{\mathrm{i}\mathbf{G}\cdot\mathbf{x}_\parallel}, \tag{S10}$$

where $\mathbf{x}_\parallel$ and $\mathbf{x}_\perp$ are the parts of $\mathbf{x} \equiv \mathbf{r} - \mathbf{r}'$ parallel and perpendicular to $\mathbf{R}_1$, respectively, and $K_0(x, y) \equiv \int_0^1 s^{-1}\mathrm{e}^{-x/s-ys}\,\mathrm{d}s$ is the so-called incomplete Bessel K function of zeroth order.[8]

As in the 2D case, the Ewald scheme also reveals the appropriate $\mathbf{k} = 0$ limit in 1D: specifically, utilizing the (generalized exponential integral) series for $K_0(x, y)$, we find that the divergent $\mathbf{G} = 0$ summand reduces to $V^{(1)}_{\mathbf{k},\mathbf{G}=0}(\mathbf{x}) = |\mathbf{R}_1|^{-1}\sum_{n=1}^{\infty}(-1)^n(Ex_\perp)^{2n}(n!n)^{-1} + \mathrm{const}_\infty = -|\mathbf{R}_1|^{-1}\{\gamma_{\mathrm{EM}} + \ln[(Ex_\perp)^2] + E_1[(Ex_\perp)^2]\} + \mathrm{const}_\infty$ with const_∞ denoting a divergent $n = 0$ contribution, which is independent of $x_\perp$ and consequently with vanishing contribution, cf. charge conservation ($\gamma_{\mathrm{EM}} \approx 0.5772156649$ is the Euler–Mascheroni constant).

C. Technical comments

1. Spurious modes

A well-known issue in discretization by linear finite elements of weak form operators is the occurrence of spurious modes [S11]. In the absence of a magnetic field, the method described here is free of spurious modes. At finite magnetic field, however, a dense band of spurious modes exists for $-\omega_c < \omega < \omega_c$. The origin of these spurious modes can be traced to numerically-induced hybridization between the trivial solutions at $\omega = 0$ and $\omega = \pm\omega_c$.[9] Fortunately, these spurious modes are largely independent of $\mathbf{k}$, i.e. dispersionless, and so can be readily identified and discarded manually. Their hybridization with non-spurious modes is weak, and decreasing with increasing mesh density: to fully eliminate any potential influence, we modelled their hybridization with the lowest non-spurious mode by a 2×2 interaction matrix, allowing us to rigorously invert and subtract spurious numerical hybridization.

2. Dipole-excited one-way edge plasmons computed in finite structures

The calculations presented in Fig. 4 are carried out in a finite structure, see Fig. S1. The domain is discretized into ∼110.000 triangular elements, distributed over ∼61.000 vertex points, with increased mesh-density along the domain periphery. To ensure that the one-way edge state is adequately attenuated over a single round-trip propagation, our "lossless" calculations in fact adopt a very small relaxation rate, $\hbar\gamma = 0.15\,\mathrm{meV}$.

---

[8] While erf and erfc are available in most special function libraries, $K_0(x, y)$ is generally not. We exploit the structure of Eq. (S10) and re-express $K_0(x, y)$ as $K_0(x, y) = \sum_{n=0}^{\infty}(-y)^n E_{n+1}(x)/n!$ in terms of the generalized exponential integrals $E_n(x)$ [obtained by Taylor expanding the integrand s of $K_0(x, y)$ around zero]. Evaluation of $E_n(x)$ are computationally expensive but are *independent of the coordinates* $\mathbf{x}_{\parallel,\perp}$; thus, they are needed only at $x = [(\mathbf{k}+\mathbf{G})\cdot\mathbf{R}_1/2E]^2$.
We choose a splitting parameter $E = [2|\mathbf{R}_1|(\max x_\perp - \min x_\perp)]^{-1}$ to effectively shift summation terms onto the short-range part, in recognizing the computational cost involved in evaluating $E_n(x)$. With this choice, reaching machine precision typically requires at most 5 reciprocal lattice vectors and $n = 0, \ldots, 10$ (but up to several hundred direct lattice vectors in $V^{(2)}_{\mathbf{k}}$ for wide ribbons).

[9] Numerically, we find that the spurious modes respect the no-spill boundary condition *globally*, i.e. are charge neutral. However, they do not respect it locally. This issue is common to many finite-element approaches, since the weak form implementation of the boundary condition only guarantees it in the integral sense, rather than the point-wise sense. A point-wise guarantee can be insured by adopting basis elements (such as RWG elements [S12]) which explicitly incorporate the boundary condition.

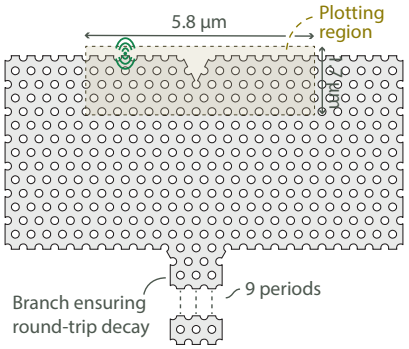

FIG. S1 Full computational geometry employed in the dipole calculations of Fig. 4. Dipole position and polarization is indicated in green. In lieu of a perfectly matched layer termination, we implement a (very) poor-man's absorber, by including an vertical branch in the structure, forcing additional decay upon the one-way propagating mode.

II. HERMICITY OF THE MAGNETOPLASMONIC EQUATIONS

Equations (1) of our Letter are, as noted briefly there, Hermitian under an appropriate inner product. In fact, the problem can be recast in a manifestly Hermitian form. In this section, we demonstrate these aspects explicitly.

A. Generalized Hermitian eigenvalue problem

In the notation of Eqs. (1), the magnetoplasmonic eigenproblem is $\hat{\mathcal{H}}\mathbf{U} = \omega\mathbf{U}$ (eigenindex suppressed) with $\mathbf{U} \equiv \begin{pmatrix} \omega_\mathrm{F}\Phi \\ \mathbf{J} \end{pmatrix} \equiv \begin{pmatrix} \tilde{\Phi} \\ \mathbf{J} \end{pmatrix}$ and $\hat{\mathcal{H}} \equiv \begin{pmatrix} 0 & \omega_\mathrm{F}\hat{V}\hat{\mathbf{p}}^\mathrm{T} \\ \alpha\mathbf{p} & \omega_\mathrm{c}\sigma_2 \end{pmatrix}$; here, $\omega_\mathrm{F} \equiv E_\mathrm{F}/\hbar$, $\alpha \equiv e^2/\pi\hbar$, $\sigma_2 \equiv \left(\begin{smallmatrix} 0 & -\mathrm{i} \\ \mathrm{i} & 0 \end{smallmatrix}\right)$, and the Coulomb ($\hat{V}$) and momentum ($\hat{\mathbf{p}}$) operators are positive-symmetric and Hermitian, respectively. Nevertheless, the compound operator $\hat{\mathcal{H}}$ is not Hermitian under the standard inner product.

However, it is straightforward to recast this problem as a generalized eigenproblem with strictly Hermitian matrices. Specifically, $\hat{\mathcal{H}}$ can be written as a product $\hat{\mathcal{H}} = \hat{\mathcal{B}}^{-1}\hat{\mathcal{A}}$ of a positive-symmetric operator $\hat{\mathcal{B}}^{-1} \equiv \begin{pmatrix} \omega_\mathrm{F}\alpha^{-1}\hat{V} & 0 \\ 0 & 1 \end{pmatrix}$ and a Hermitian operator $\hat{\mathcal{A}} \equiv \begin{pmatrix} 0 & \alpha\hat{\mathbf{p}}^\mathrm{T} \\ \alpha\hat{\mathbf{p}} & \omega_\mathrm{c}\sigma_2 \end{pmatrix}$. Thus, there exists an equivalent formulation as a generalized eigenvalue problem

$$\hat{\mathcal{A}}\mathbf{U} = \omega\hat{\mathcal{B}}\mathbf{U}, \qquad \text{with} \quad \hat{\mathcal{B}} = \begin{pmatrix} \alpha\omega_\mathrm{F}^{-1}\hat{V}^{-1} & 0 \\ 0 & 1 \end{pmatrix}, \tag{S11}$$

where $\mathcal{B}$ is positive-symmetric (the inverse of a symmetric operator is symmetric). Thus, Eq. (S11) is a generalized Hermitian eigenproblem with Hermitian definite pencil $\{\hat{\mathcal{A}}, \hat{\mathcal{B}}\}$ [S13]: accordingly, its eigenvalues are real and its states are orthogonal under the inner product[10] $\langle \mathbf{U}_\nu | \mathbf{U}_{\nu'} \rangle \equiv \int \mathbf{U}_\nu^\dagger(\mathbf{r})\hat{\mathcal{B}}\mathbf{U}_{\nu'}(\mathbf{r})\,\mathrm{d}^2\mathbf{r} \propto \delta_{\nu\nu'}$. Under this inner product, the states of Eqs. (1), which are equivalent to those of Eq. (S11), have well-defined Chern numbers. Similarly, the original "Hamiltonian" $\hat{\mathcal{H}}$ is Hermitian under this inner product. In fact, as we show in the following, the problem can be equivalently cast in a manifestly Hermitian form.

B. Manifestly Hermitian eigenvalue problem

A generalized Hermitian eigenproblem can be cast in manifestly Hermitian form if the square root of either of the operators is well-defined. Specifically, for a positive-definite symmetric operator, such as $\hat{V}$ (and hence $\hat{\mathcal{B}}$), its square root is well-defined and unique: thus, there exists a factorization $\hat{V} \equiv \hat{L}\hat{L}^\dagger$. In

[10] The inverse Coulomb operation $\hat{V}^{-1}$ acting onto the total potential Φ simply produces the the charge density ρ.

real-space coordinates, this translates to the statement that (here, anticipating that $L(\mathbf{r},\mathbf{r}')$ is real)

$$V(\mathbf{r},\mathbf{r}') \equiv \int L(\mathbf{r},\mathbf{r}'')L(\mathbf{r}',\mathbf{r}'')\,\mathrm{d}^2\mathbf{r}''. \tag{S12}$$

In fact, since $V(\mathbf{r},\mathbf{r}')$ depends strictly on $|\mathbf{r}-\mathbf{r}'|$, this is equivalent to the convolution $V(\mathbf{r}-\mathbf{r}') \equiv \int L(\mathbf{r}-\mathbf{r}'')L(\mathbf{r}''-\mathbf{r}')\,\mathrm{d}^2\mathbf{r}''$. For the Coulomb operator, $V(\mathbf{r}-\mathbf{r}') = |\mathbf{r}-\mathbf{r}'|^{-1}$, one can show[11] that $L(\mathbf{r}-\mathbf{r}') \propto |\mathbf{r}-\mathbf{r}'|^{-3/2}$ (i.e. it is positive-symmetric, and $\hat{L}\hat{L}^\dagger = \hat{L}\hat{L}$, rendering Hermitian conjugation unnecessary).

The factorization of $\hat{V}$, translates directly to a factorization of $\hat{\mathcal{B}}$, specifically, $\hat{\mathcal{B}} = \hat{\mathcal{L}}\hat{\mathcal{L}}$ with $\hat{\mathcal{L}} \equiv \begin{pmatrix} \sqrt{\alpha/\omega_\mathrm{F}}\hat{L} & 0 \\ 0 & 1 \end{pmatrix}$. The generalized eigenvalue problem of Eq. (S11) can then be written as $\hat{\mathcal{A}}\mathbf{U} = \omega\hat{\mathcal{L}}\hat{\mathcal{L}}\mathbf{U}$; a manifestly Hermitian eigenproblem follows by inserting unity in the form of $\hat{\mathcal{L}}^{-1}\hat{\mathcal{L}}$ and left-multiplying by $\hat{\mathcal{L}}^{-1}$:

$$\hat{\mathcal{H}}'\mathbf{U}' = \omega\mathbf{U}', \qquad \text{with} \quad \hat{\mathcal{H}}' \equiv \hat{\mathcal{L}}^{-1}\hat{\mathcal{A}}\hat{\mathcal{L}}^{-1} \text{ and } \mathbf{U}' \equiv \hat{\mathcal{L}}\mathbf{U}. \tag{S13}$$

In explicit terms, the manifestly Hermitian system has Hamiltonian $\hat{\mathcal{H}}'$ and eigenstates $\mathbf{U}'$

$$\hat{\mathcal{H}}' = \begin{pmatrix} 0 & \sqrt{\alpha\omega_\mathrm{F}}\hat{L}^{-1}\hat{\mathbf{p}}^\mathrm{T} \\ \sqrt{\alpha\omega_\mathrm{F}}\hat{\mathbf{p}}\hat{L}^{-1} & \omega_\mathrm{c}\sigma_2 \end{pmatrix}, \qquad \mathbf{U}' = \begin{pmatrix} \sqrt{\alpha\omega_\mathrm{F}}\hat{L}\Phi \\ \mathbf{J} \end{pmatrix}, \tag{S14}$$

which is evidently Hermitian since $\hat{\mathcal{L}}^\dagger = \hat{\mathcal{L}}$. This new manifestly Hermitian Hamiltonian $\hat{\mathcal{H}}'$ relates with the original, non-Hermitian Hamiltonian $\hat{\mathcal{H}}$ of Eqs. (1) by $\hat{\mathcal{H}}' = \hat{\mathcal{L}}\hat{\mathcal{H}}\hat{\mathcal{L}}^{-1}$. The eigenstates $\mathbf{U}'$ are orthogonal under the conventional inner product $\langle\mathbf{U}'_\nu|\mathbf{U}'_{\nu'}\rangle' \equiv \int \mathbf{U}'^\dagger_\nu(\mathbf{r})\mathbf{U}'_{\nu'}(\mathbf{r})\,\mathrm{d}^2\mathbf{r}$ (which, unsurprisingly, is equivalent to the previously defined inner product for non-primed states, since $\mathbf{U}'^\dagger\mathbf{U}' = \mathbf{U}^\dagger\hat{\mathcal{L}}\hat{\mathcal{L}}\mathbf{U} = \mathbf{U}^\dagger\hat{\mathcal{B}}\mathbf{U}$).

C. Generalization to the nonuniform case

The considerations outlined above can be generalized to the case where ω_F and ω_c are $\mathbf{r}$-dependent, i.e. with non-uniform doping. We need to first define a new set of state functions,

$$\mathbf{S} \equiv \begin{pmatrix} \sqrt{\omega_\mathrm{F}(\mathbf{r})}\Phi \\ \mathbf{J}/\sqrt{\omega_\mathrm{F}(\mathbf{r})} \end{pmatrix}, \quad \omega\mathbf{S} = \begin{pmatrix} 0 & \frac{1}{\sqrt{\omega_\mathrm{F}}}\hat{V}\hat{\mathbf{p}}^\mathrm{T}\sqrt{\omega_\mathrm{F}(\mathbf{r})} \\ \frac{\alpha}{\sqrt{\omega_\mathrm{F}}}\sqrt{\omega_\mathrm{F}(\mathbf{r})}\hat{\mathbf{p}} & \omega_\mathrm{c}(\mathbf{r})\sigma_2 \end{pmatrix}\mathbf{S}, \tag{S15}$$

where ω_F is the value of $\omega_\mathrm{F}(\mathbf{r})$ in the uniform region. Then we have

$$\hat{\mathcal{A}}\mathbf{S} = \omega\hat{\mathcal{B}}\mathbf{S}, \quad \text{with} \quad \hat{\mathcal{A}} = \begin{pmatrix} 0 & \frac{\alpha}{\sqrt{\omega_\mathrm{F}}}\hat{\mathbf{p}}^\mathrm{T}\sqrt{\omega_\mathrm{F}(\mathbf{r})} \\ \frac{\alpha}{\sqrt{\omega_\mathrm{F}}}\sqrt{\omega_\mathrm{F}(\mathbf{r})}\hat{\mathbf{p}} & \omega_\mathrm{c}(\mathbf{r})\sigma_2 \end{pmatrix}, \quad \hat{\mathcal{B}} = \begin{pmatrix} \alpha\omega_\mathrm{F}(\mathbf{r})^{-1}\hat{V}^{-1} & 0 \\ 0 & 1 \end{pmatrix}. \tag{S16}$$

Because $\hat{\mathbf{p}}$ and $\omega_\mathrm{F}(\mathbf{r})$ do not commute, their order appearing in $\hat{\mathcal{A}}$ matters. $\hat{\mathcal{B}}$ is exactly the same as above, so similar treatment can be straightforwardly performed. With $\mathbf{S}' \equiv \hat{\mathcal{L}}\mathbf{S}$, the manifest Hermitian Hamiltonian looks like

$$\hat{\mathcal{H}}'\mathbf{S}' = \omega\mathbf{S}', \quad \text{with} \quad \hat{\mathcal{H}}' = \begin{pmatrix} 0 & \hat{L}^{-1}\hat{\mathbf{p}}^\mathrm{T}\sqrt{\alpha\omega_\mathrm{F}(\mathbf{r})} \\ \sqrt{\alpha\omega_\mathrm{F}(\mathbf{r})}\hat{\mathbf{p}}\hat{L}^{-1} & \omega_\mathrm{c}(\mathbf{r})\sigma_2 \end{pmatrix}. \tag{S17}$$

Finally, the above considerations, in both uniform and non-uniform cases, generalize immediately to the parabolic 2D electron gas of effective mass m^* and density n_0 under the substitutions $\omega_\mathrm{F} \to \hbar\pi n_0/m^*$ and $\omega_\mathrm{c} \to eB/cm^*$.

---

[11] The explicit expression for $L(\mathbf{r}-\mathbf{r}')$ can be obtained by exploiting the convolution theorem. In Fourier space (i.e. momentum space, $\mathbf{q}$), the convolution is a product $V(\mathbf{q}) = L(\mathbf{q})L(\mathbf{q})$. Conversely, the Coulomb interaction in 2D momentum space is $V(\mathbf{q}) = 2\pi/q$, thus fixing $L(\mathbf{q}) = \sqrt{2\pi/q}$. Accordingly, the real-space form $L(\mathbf{r}-\mathbf{r}')$ can be evaluated by an inverse Fourier transform [S14]

$$L(\mathbf{r}-\mathbf{r}') = \int U(\mathbf{q})\mathrm{e}^{\mathrm{i}\mathbf{q}\cdot(\mathbf{r}-\mathbf{r}')}\frac{\mathrm{d}^2\mathbf{q}}{(2\pi)^2} = \frac{s^{-1}}{|\mathbf{r}-\mathbf{r}'|^{3/2}},$$

where $s = 5.2441\ldots$ is the Lemniscate constant (alternatively, $s \equiv \Gamma(1/4)^2/\sqrt{2\pi}$ in terms of the Gamma function).

III. ADDITIONAL BAND STRUCTURE RESULTS

In order to clearly visualize the Dirac cones, point degeneracies, and band gaps of the full band structures, we computed the energy dispersion $\hbar\omega_n(\mathbf{k})$ over the entire 2D Brillouin zone (BZ). Figure S2 illustrates the resulting band structure for $a = 400\,\text{nm}$, $d = 200\,\text{nm}$, and $B = 0,\ 4,$ and $8\,\text{T}$. All the extrema of the bands are observed to lie on the boundary of the irreducible BZ.

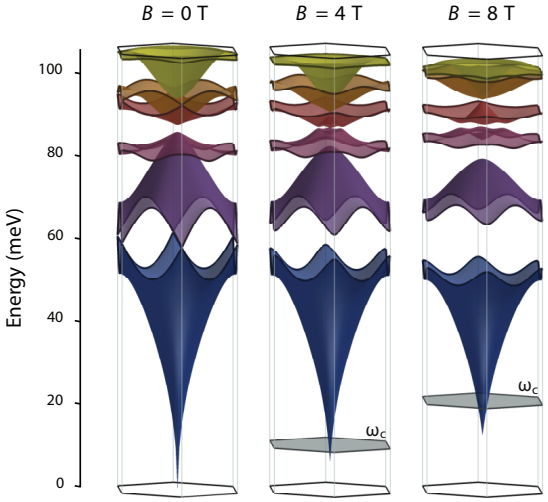

FIG. S2 Plasmonic bulk dispersion $\hbar\omega_n(\mathbf{k})$ of the first six bands over the entire BZ (indicated) for the triangular antidot lattice considered in Fig. 2 ($a = 400\,\text{nm}$, $d = 200\,\text{nm}$, and $E_\text{F} = 0.2\,\text{eV}$), across varying magnetic field strengths B. For nonzero B, the associated cyclotron frequency is indicated by a gray plane.

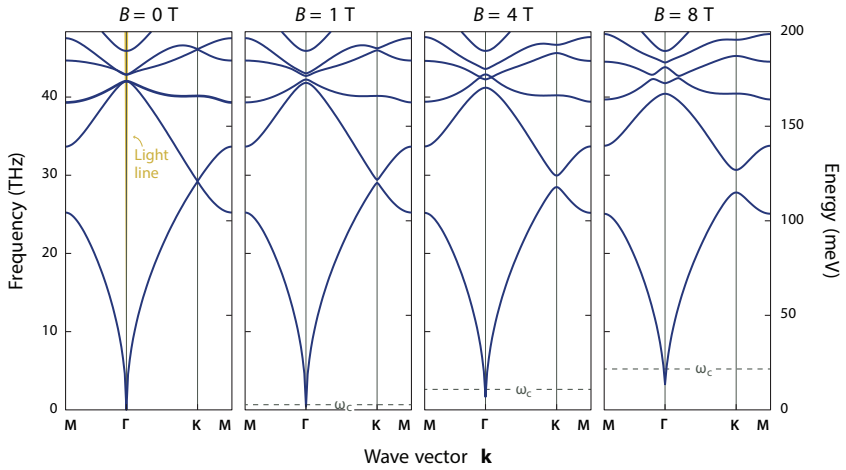

FIG. S3 Plasmonic bulk dispersion along the boundary of the irreducible BZ of a triangular lattice. Setup parameters mirror those of Fig. 2 but at quarter scale, i.e. with period $a = 100\,\text{nm}$ and antidot diameter $d = 50\,\text{nm}$.

To illustrate the impact of reducing the overall scale of the triangular lattice, we depict in Fig. S3 the result of a calculation at one quarter the scale of those in the main text, i.e. at $a = 100\,\text{nm}$ and $d = 50\,\text{nm}$. In the absence of a magnetic field, the one-quarter scale reduction simply results in a doubling of all resonance frequencies, consistent with the $\hbar\omega_n \propto \sqrt{1/a}$ intraband scaling law. For nonzero B, the scaling law is strictly speaking broken—qualitatively, however, the changes are few; amounting mainly to a reduction in gap-midgap ratio, since the gap width mainly depends on the amplitude of $\mathcal{T}$ breaking (magnitude $\sim\omega_\text{c}$).

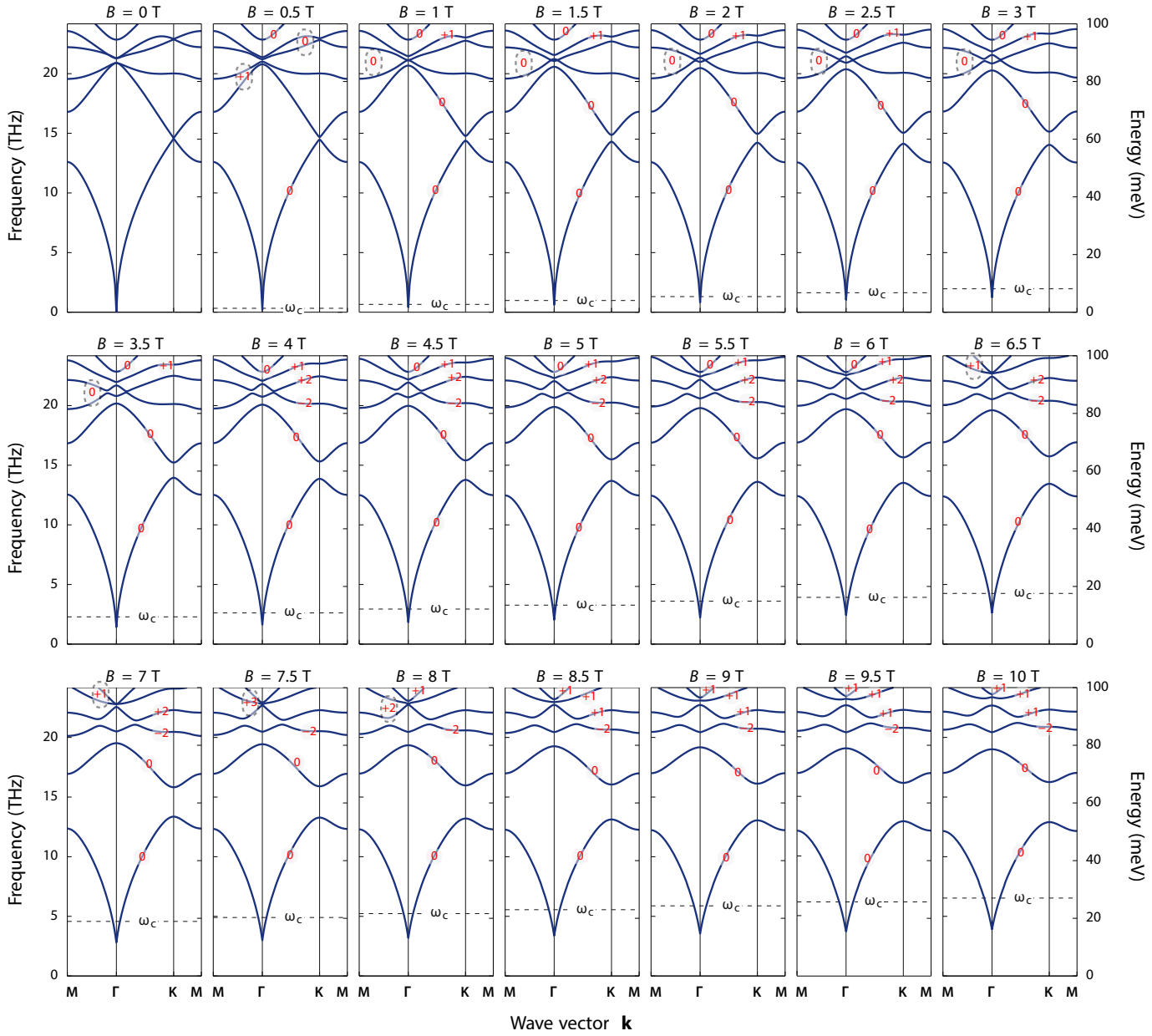

FIG. S4 Evolution of plasmonic bulk dispersion (blue) and Chern numbers (orange numbers) with increasing magnetic field B for the crystal considered in Fig. 2 ($a = 400\,\text{nm}$, $d = 200\,\text{nm}$, and $E_\text{F} = 0.2\,\text{eV}$). Composite Chern numbers are indicated by a dashed periphery.

IV. CHERN NUMBER EVOLUTION WITH MAGNETIC FIELD

If the nth band is well-separated (i.e. everywhere non-degenerate) from all other bands, it can be assigned a (first) Chern number

$$C^{(n)} \equiv \frac{1}{2\pi\mathrm{i}} \oint_{\partial\mathrm{BZ}} \langle \mathbf{u}_{n\mathbf{k}} | \nabla_{\mathbf{k}} | \mathbf{u}_{n\mathbf{k}} \rangle \, \mathrm{d}\mathbf{k}, \tag{S18}$$

where $|\mathbf{u}_{n\mathbf{k}}\rangle$ is the normalized eigenstate of momentum $\mathbf{k}$ in the nth band. The inner product defined with weighting $\hat{\mathcal{B}}$ as discussed in Section II, and can be performed in coordinate-space over a single unit cell.

For s bands with shared degeneracies, we calculate the composite (first) Chern number as [S15]

$$C^{(n\oplus n+1\oplus\cdots\oplus n+s-1)} \equiv \det M_{\mu\nu} \equiv \frac{1}{2\pi\mathrm{i}} \det\Big(\oint_{\partial\mathrm{BZ}} \langle \mathbf{u}_{\mu\mathbf{k}} | \nabla_{\mathbf{k}} | \mathbf{u}_{\nu\mathbf{k}} \rangle \, \mathrm{d}\mathbf{k} \Big), \quad (\mu,\nu = n, n+1, \ldots, n+s-1). \tag{S19}$$

The composite Chern number is the determinant of an $s \times s$ matrix with elements $M_{\mu\nu}$, i.e. includes cross-terms between distinct bands. With these definitions, the (composite) Chern numbers are evaluated numerically following the standard $\mathbf{k}$-discretization scheme by Fukui *et al.* [S16].

The calculation of $C^{(1)}$ requires special care due to since the $\omega_1(\mathbf{k})$ dispersion exhibits a square-root non-differentiable singularity at the $\mathbf{\Gamma}$ point. This singularity originates from the infinitely ranged Coulomb interaction and produces a divergent Berry curvature at the $\mathbf{\Gamma}$ point. To remedy this (unphysical) issue, we substitute a screened (Yukawa) interaction for the bare Coulomb interaction, thereby introducing a finite (but large) range l to the electrostatic interaction: specifically, $1/r \to \mathrm{e}^{-r/l}/r$ with $l \gg a$. This treatment yields the correct Chern number $C^{(1)} = 0$, reflecting the cancellation between $+1$ and -1 monopoles of Berry flux at the $\mathbf{\Gamma}$ and $\mathbf{K}$ points, respectively. We emphasize that the the first band's vanishing Chern number, $C^{(1)} = 0$, still implies nontrivial topology at the gaps above and below the first band, cf. Eq. (2).

Lastly, we observe that both the energy dispersion and Chern numbers of the plasmonic crystal exhibit an interesting evolution as the applied magnetic field is gradually increased; of special interest is band openings and closings, where the topological band classification may change. This is illustrated in Fig. S4 for the crystal considered in Fig. 2 of our Letter: the band dispersion and Chern number evolution is recorded as the magnetic field is varied from $B = 0$ to 10 T in steps of 0.5 T, producing several changes to the topological band indices via the exchange of monopoles of Berry flux at band openings and closings.

V. INTERBAND DISPERSION AND LANDAU DAMPING

Besides plasmons, the elementary excitations of graphene include intra- and interband electron-hole pair (EHP) excitations. In regions where both co-exist, plasmons decay into EHPs in the process known as Landau damping. In graphene, the plasmon branch enters the continuum of interband EHPs at high energies and momenta, and undergoes rapid damping. Clearly, this poses an important restriction on the relevant energy-momentum range for both topological and non-topological graphene plasmons. Here, we briefly discuss this restriction and show that our system is far from regions of Landau damping.

Interband EHPs in extended graphene — We first indicate the energy-momentum interrelation required for the excitation of interband EHPs by graphene plasmons. For an electron-doped sheet, $E_\mathrm{F} > 0$, an electron can make a transition from the negative- to positive-frequency band, i.e. from $(\mathbf{k}', \omega' < 0)$ to $(\mathbf{k}'', \omega'' > 0)$, provided it complies with the Pauli exclusion principle and the electron band dispersion $E(\mathbf{k}) = \hbar v_\mathrm{F}|\mathbf{k}|$. This requires a frequency transfer $\omega(\mathbf{q}) = \omega'' - \omega' > E_\mathrm{F}/\hbar - \omega'$ and a momentum transfer $\mathbf{q} = \mathbf{k}'' - \mathbf{k}'$. Depending on the initial state's frequency and the alignment between $\mathbf{k}'$ and $\mathbf{k}''$, a range of $(\mathbf{q}, \omega)$ are consistent with these requirements: jointly, they form a region where interband EHPs can be excited, as illustrated in Fig. S5(a).

Supposing the necessary momentum and energy transfer is provided by a plasmon, further restrictions are imposed by the momentum-energy dispersion $\omega(\mathbf{q})$ of the plasmon. Specifically, a plasmon-induced transition is possible if $\omega(\mathbf{q}) = v_\mathrm{F}(|\mathbf{k}''| + |\mathbf{k}'' - \mathbf{q}|)$. If $\mathbf{k}'$ and $\mathbf{q}$ align, i.e. if $|\mathbf{k}'| = |\mathbf{k}'' - \mathbf{q}| = |\mathbf{k}''| - |\mathbf{q}|$, we obtain the minimal necessary momentum transfer as $\omega(\mathbf{q}) = v_\mathrm{F}(2|\mathbf{k}''| - |\mathbf{q}|)$. The Pauli principle requires $|\mathbf{k}''| > E_\mathrm{F}/\hbar v_\mathrm{F}$, thus indicating the minimum-momentum-transfer condition for interband plasmon damping:

$$\hbar\omega(\mathbf{q}) + \hbar v_\mathrm{F}|\mathbf{q}| > 2E_\mathrm{F}. \tag{S20}$$

To approximately ascertain this region's extent, we exploit our knowledge of the low-frequency (i.e. intraband approximation) of graphene's plasmon dispersion $\hbar\omega(\mathbf{q}) \simeq \sqrt{2e^2 E_\mathrm{F}|\mathbf{q}|}$ to eliminate E_F in Eq. (S20), allowing identification of an approximate $(\mathbf{q}, \omega)$ region wherein plasmons decay into interband EHPs:

$$\omega + v_\mathrm{F}|\mathbf{q}| > \frac{\hbar\omega^2}{e^2|\mathbf{q}|}. \tag{S21}$$

By adopting a representative plasmon momentum $|\mathbf{q}| \to 4\pi/3a$ (corresponding to the $\mathbf{K}$ point in the Brillouin zone of a triangular lattice of period a) Fig. 1(c) employs this result to approximately delineate the parameter-region where interband dispersion significantly impacts our intraband treatment.

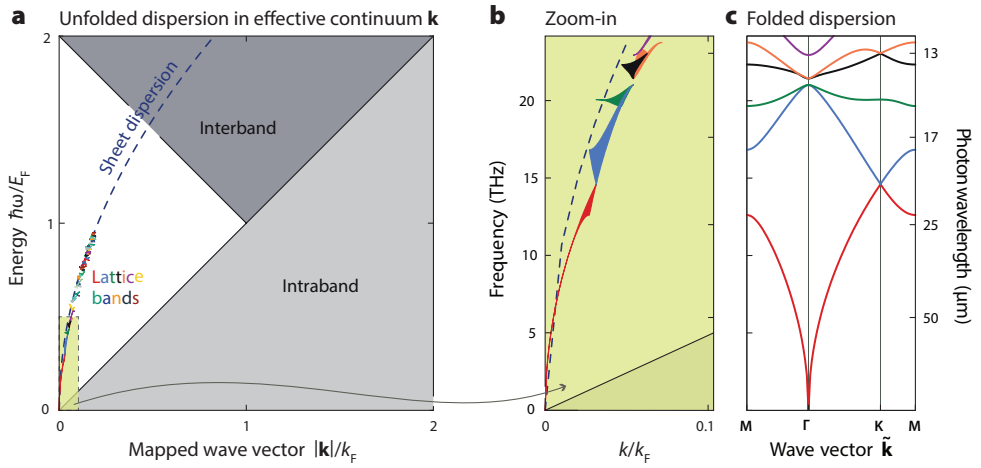

FIG. S5 The plasmonic dispersion of the graphene antidot lattice considered in Fig. 2, unfolded onto continuum wave vectors, via an inverse application of the empty-lattice approximation. (a) Unfolded dispersion of the antidot lattice in multicolored patches (delimited by the dispersion over the irreducible BZ) along the dispersion of the extended sheet (dashed blue) in the intra- and interband EHP landscape of extended graphene. (b) Zoom-in on the energy range considered in Fig. 2. (c) Folded dispersion of the antidot lattice over the irreducible BZ.

Unfolded band-dispersion — Because of band-folding, the plasmonic excitations of antidot lattices cannot be rigorously mapped to the excitations of the extended graphene sheet. Specifically, in the former (lattices) plasmonic states are indexed by the band index n and the reduced wave vector $\tilde{\mathbf{k}} \in \mathrm{BZ}$, whereas in the latter (pristine graphene) the unrestricted wave vector $\mathbf{k} \in \mathbb{R}^2$ suffices. The preceding discussion of interband transitions evidently adopts the latter perspective, and so, strictly speaking, does not apply to lattices. Indeed, a lattice plasmon is composed of a range of momenta $\{\mathbf{k} + \mathbf{G}\}$, spanned by the reciprocal lattice vectors $\{\mathbf{G}\}$. Nevertheless, the empty-lattice approximation suggests that each state is predominately in a specific momentum state: specifically, turning the empty-lattice approximation on its head, we can approximately map a lattice state $(n, \tilde{\mathbf{k}})$ to an extended state $\mathbf{k} \sim \tilde{\mathbf{k}} + \mathbf{G}_n$ with $\mathbf{G}_n$ denoting the nth *sorted* reciprocal lattice vector (in the sense $|\tilde{\mathbf{k}} + \mathbf{G}_1| < |\tilde{\mathbf{k}} + \mathbf{G}_2| < |\tilde{\mathbf{k}} + \mathbf{G}_3| < \ldots$). This allows us to gauge the lattice plasmons' distance from regions of severe Landau damping.

Figure S5 depicts the result of such a procedure: each folded band $\omega_n(\tilde{\mathbf{k}})$ is approximately "unfolded" onto the continuum wave vector and compared with the extended sheet's dispersion. The validity of the procedure is well-illustrated by the overlap between the two. Further, the lattice bands evidently lie far from the regime of interband EHP production in the relevant energy range: this demonstrates that our intraband treatment is fully sufficient in the considered parameter space.

VI. NONCLASSICAL REGIME OF LANDAU QUANTIZATION

Under a perpendicular magnetic field B, the Dirac electrons of graphene undergo Landau quantization [S17]

$$E_{\mathrm{L}}(\nu) \equiv \hbar\omega_{\mathrm{L}}(\nu) = \pm v_{\mathrm{F}} \sqrt{\frac{2\hbar e B}{c}}\, \sqrt{\nu}, \quad \nu = 0, 1, 2, \ldots \tag{S22}$$

We consider positive Fermi energy, and hence restrict ourselves to the positive-energy levels. Each such level contains a large degeneracy g proportional to the magnetic flux Φ over the sample:

$$g = 4\frac{\Phi}{\Phi_0} = 4\frac{BS}{\Phi_0}, \tag{S23}$$

where the factor of 4 sums the spin and valley degeneracies, S is the sample area, and $\Phi_0 = 2\pi\hbar c/e$ is the flux quantum.

At a specified B field, the Fermi level E_{F} may coincide with a level or lie in a gap between levels. Depending on the impurity concentration and the temperature, in the static limit, the system may exhibit classical

or quantum Hall effect. At finite frequencies, transitions among different Landau levels can occur and a quantum treatment is appropriate [S3]. However, under the following condition, a semiclassical description suffices to describe the dynamic response [S3; S4]:

$$E_{\rm F} > \hbar\omega_{\rm L}(\nu = 1) = v_{\rm F}\sqrt{\frac{2\hbar eB}{c}}, \tag{S24}$$

Under this condition, the response is well-described by the semiclassical treatment adopted in our Letter, i.e. by the cyclotron motion at frequency[12] $\omega_{\rm c} = eBv_{\rm F}^2/cE_{\rm F}$. Equation (S24) can be recast as an equivalent restricting condition on the magnitude of $\omega_{\rm c}$:

$$\omega_{\rm c} < \frac{v_{\rm F}}{\hbar}\sqrt{\frac{\hbar eB}{2c}} = \tfrac{1}{2}\omega_{\rm L}(\nu = 1). \tag{S25}$$

Thus, the semiclassical framework is representative of the full quantum mechanical response provided the cyclotron energy is less than one half of the first Landau level. In turn, this requires that $E_{\rm F}$ is not too small and B is not too large. The region where this condition is violated is indicated in Fig. 1(c) of our Letter as the region of Landau quantization.

Finally, we note the existence of a distinct class of magnetoplasmons, theoretically predicted in undoped (or very weakly doped; ~ 1 filled Landau levels) pristine graphene under very large magnetic fields [S18; S19]. This class of magnetoplasmons involve a few interacting electron-hole pairs, discretized into well-separated Landau levels, oscillating around the Dirac point. We emphasize that this class of magnetoplasmons, which exist in the extreme quantum Hall regime $E_{\rm F} \ll \hbar\omega_{\rm c}$, is starkly different from the class considered in this Letter [S19]—the latter class is well-described by a semiclassical treatment and are of a magnetohydrodynamic character; the conventional plasmon "dressed" by the magnetic field. Microscopically, they are composed of a large number of interacting electron-hole pairs excited around high-lying, densely spaced Landau levels such that $E_{\rm F} \gg \hbar\omega_{\rm c}$. In contrast, the large-B, small-$E_{\rm F}$ magnetoplasmons studied in Ref. S18 reside in the opposite domain and have no $B \to 0$ analogue [S19].

VII. INFLUENCE OF FINITE LOSS

The influence of finite intrinsic loss, due to a Drude relaxation rate γ, was discussed in our Letter and quantified in Fig. 4(e). Here, we elaborate on these aspects, obtaining along the way universal scaling laws which hold implications also for the lossless scenario.

A. Scaling laws and perturbative considerations

Absence of magnetic field— As discussed in Section I.A, the resonances of a 2D nanostructure Ω with an isotropic conductivity $\sigma(\omega)$ and of characteristic length L are dictated by a set of dimensionless eigenvalues $\zeta_\nu \equiv {\rm i}\omega_\nu L/2\pi\sigma(\omega_\nu)$ which depend solely on the *shape* of Ω and the modal index ν. Within an intraband treatment of graphene, $\sigma(\omega) = \frac{{\rm i}\alpha\omega_{\rm F}}{\omega+{\rm i}\gamma} = \frac{{\rm i}e^2E_{\rm F}}{\pi\hbar^2(\omega+{\rm i}\gamma)}$, the resonant frequencies can be obtained explicitly as:

$$\omega_\nu = \sqrt{(\omega_\nu^0)^2 + \tfrac{1}{4}\gamma^2} - \tfrac{\rm i}{2}\gamma, \qquad \text{with } \omega_\nu^0 = \sqrt{2\pi\alpha\omega_{\rm F}\zeta_\nu/L}, \tag{S26}$$

simplifying to $\omega_\nu \simeq \omega_\nu^0 - {\rm i}\gamma/2$ for $\omega_\nu^0 \gg \gamma$. Thus, within the isotropic ($B = 0$) intraband description, *every* plasmonic state, whether bulk-like, edge-like, or localized, has an imaginary spectral component ${\rm Im}\,\omega_\nu = -\gamma/2$. On the other hand, the real component ${\rm Re}\,\omega_\nu \simeq \omega_\nu^0$ depends on modal index ν, geometric length scale L, and Fermi level $\omega_{\rm F}$ [in the plasmonic lattices considered here $\nu = (n, \mathbf{k} \in {\rm BZ})$ and $L = a$].

---

[12] The semiclassical cyclotron description can be slightly improved by substituting the cyclotron frequency $\omega_{\rm c}$ for the energy-gap across the Fermi energy $\omega_{\rm L}(\nu_{\rm F}+1) - \omega_{\rm L}(\nu_{\rm F})$ with $\nu_{\rm F}$ denoting the highest filled Landau level [S4]. In the limit $\nu_{\rm F} \gg 1$ the cyclotron frequency is recovered. This sophistication (which we do not include in our calculations) amounts to a small rescaling of the cyclotron frequency, on the order of 1.5% for $B = 8\,{\rm T}$ and $E_{\rm F} = 0.2\,{\rm eV}$.

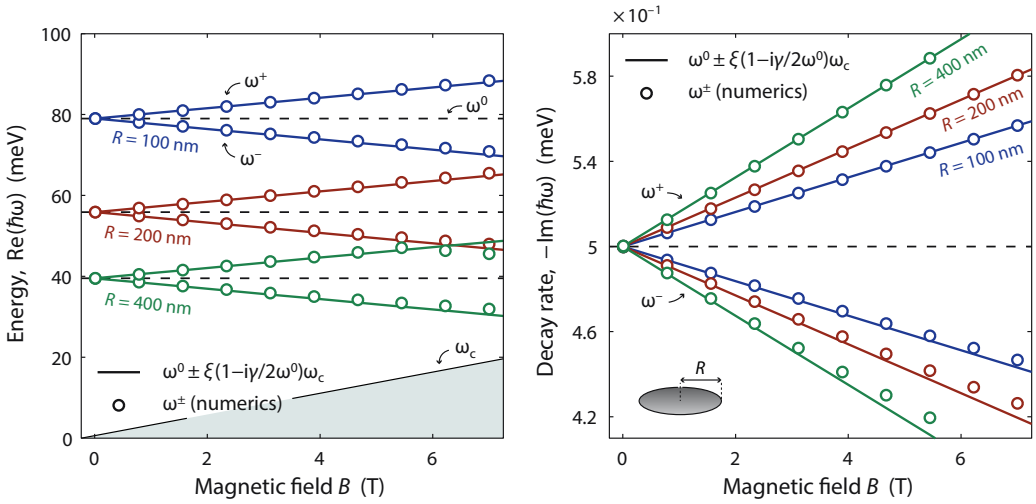

FIG. S6 Splitting of the dipole modes of a graphene nanodisk ($E_F = 0.2$ eV and $\hbar\gamma = 1$ meV) of radii $R = 100,\ 200,$ and 400 nm under a finite magnetic field. The dipole modes are split into co- and counter-rotating (ω^- and ω^+) dipole modes. The initially degenerate modes are evenly split, such that $\delta\omega^\pm = \pm\xi(1 - i\gamma/2\omega^0)\omega_c$ with $\xi \approx 0.475$.

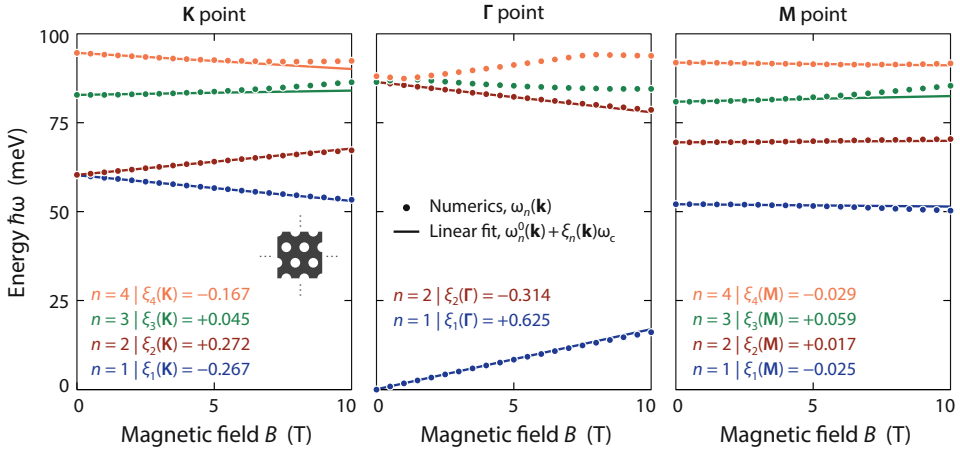

FIG. S7 Spectral shifting under the application of a finite B-field in the triangular antidot lattice considered in Fig. 2 (assuming zero loss). The plasmonic frequencies $\hbar\omega_n(\mathbf{k})$ are plotted as a function of applied B-field at wave vectors corresponding to the **K**, **Γ**, and **M** points. The associated modal coefficients $\xi_n(\mathbf{k})$ are indicated. The $n = 3$ and 4 bands at **Γ** undergo a band-closing and are consequently not well-described by Eq. (S27).

Perturbative impact of a finite magnetic field— The application of a finite magnetic field breaks the simple scaling law in Eq. (S26). Nevertheless, for small magnetic fields, $\omega_c \ll \omega_\nu$, the problem can be treated perturbatively. We leave out the details and simply state the end-result: the $B = 0$ eigenspectrum ω_ν is shifted to the $B \neq 0$ spectrum $\omega_\nu + \delta\omega_\nu + O(\omega_c^2/\omega_\nu^2)$ with the first-order correction

$$\delta\omega_\nu = \xi_\nu \frac{\omega_c \omega_\nu}{\omega_\nu + i\gamma/2} \simeq \xi_\nu(1 - i\gamma/2\omega_\nu^0)\omega_c, \tag{S27}$$

assuming small loss at the second equality. ξ_ν is a dimensionless modal parameter analogous to ζ_ν, depending solely on the shape of Ω and the modal index ν; it can be computed either from the eigenstates of the non-perturbed problem, or, more pragmatically and simply, by fitting to explicit calculations.

Adopting the fitting-approach, we illustrate these perturbation results in Figs. S6 and S7 and compare with full calculations for finite magnetic fields. Fig. S6 considers the (real and imaginary) splitting of the co- and counter-rotating dipole modes of a simple disk, while Fig. S7 considers the (real) spectral shifts of the triangular antidot lattice at the **K**, **Γ**, and **M** points. Both clearly illustrate that the $B \neq 0$ induced shifts are well-described by the linear result in Eq. (S27), even for moderately large magnetic fields. Evidently, the

plasmonic loss rate is not significantly altered from its $B = 0$ value even at $B \neq 0$ since $\omega_c \ll \omega_\nu^0$.

B. Ribbon spectrum under finite loss: spectral density from numerical calculations

To complement the preceding analytical considerations, we also performed fully numerical calculations of the complex eigenspectrum $\omega_n(k_x)$ in 1D periodic antidot lattices (i.e. ribbons) under finite relaxation. A ribbon extended along x and finite along y (20 unit cells) is considered, see Fig. S8(a); this system, in a lossless configuration, also underlies the semi-infinite sheet' edge dispersion discussed in Fig. 3 of our Letter (with half the edge states). To simultaneously depict the mode-broadening and the band dispersion, i.e. both real and imaginary parts of $\omega_n(k_x)$, we consider the spectral function

$$A(k_x, \omega) \equiv -\frac{1}{\pi} \sum_n \frac{1}{\omega - \omega_n(k_x)}, \tag{S28}$$

which defines the spectral density of states $\mathrm{Im}\, A(k_x, \omega)$ depicted in Figs. S8(b–d). The resulting intensity maps depict both bulk and edge modes (propagating on either side of the ribbon, in opposite directions); the bulk modes are discretized into a finite number of bands, reflecting the finite extent of the ribbon. Edge modes exist in the gaps between bulk regions. Finite relaxation rates, considered here in the range $\hbar\gamma = 0.5$, 2, and 6 meV, broadens the spectral features of bulk and edge states, as expected from the discussion in the preceding section. At high loss, the band gaps are severely blurred indicating its effective removal. Thus, large intrinsic relaxation necessitates correspondingly large B-fields to maintain well-defined bandgaps.

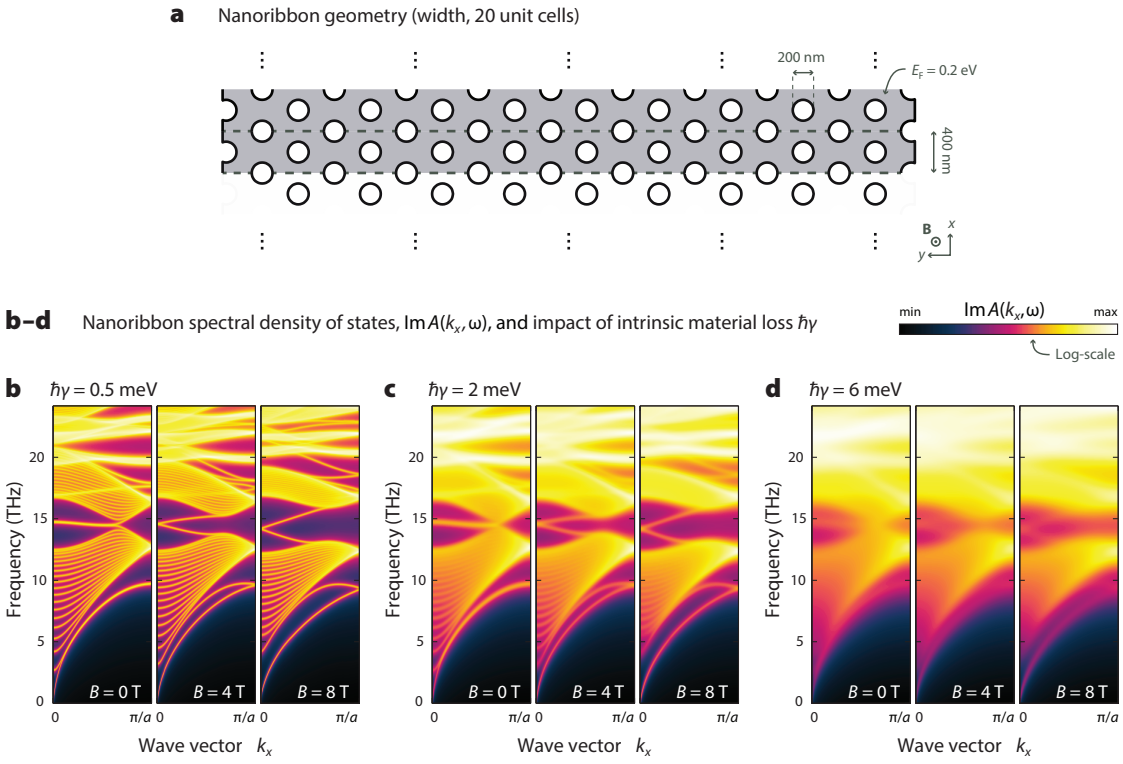

FIG. S8 Spectral density of states, $\mathrm{Im}\, A(k_x, \omega)$, of an antidot ribbon under an applied magnetic field $B = 0,\ 4,$ and 8 T for varying relaxation rates $\hbar\gamma = 0.5,\ 2,$ and 6 meV. (a) Ribbon setup. (b-d) Spectral density of states.

C. Dipole-excited one-way propagation under finite loss

To complement the results of Fig. 4(e), we present in Fig. S9 additional results on the impact of intrinsic loss on propagation of the $\bar{C}^{(1)}$ gap edge plasmons, for lattice constants $a = 400$ and 100 nm and $\hbar\gamma = 1,\ 2,$

and 4 nm. These results demonstrate that the effective propagation length l/a can be dramatically enhanced at smaller lattice constants. This reveals the existence of a trade-off between gap–midgap ratio ($\propto \omega_c/\sqrt{a}$, i.e. preferring large a) and effective propagation length (preferring small a). Since the gap–midgap ratio is less important in plasmonic applications than in e.g. photonic crystal applications (where bandwidth is central figure of merit), this trade-off allows additional design-flexibility. A similar trade-off may be feasible by increasing E_F, though at a steeper cost to the gap–midgap ratio.

Figures 4(e) and S9 also demonstrate that the effective propagation length improves with increasing magnetic field B. This B-dependence is chiefly due to an increased edge plasmon group velocity, which is roughly proportional to the gap magnitude. More generally, by maximizing the edge plasmon group velocity the effective propagation length can be enhanced. This can achieved by separately optimizing the lattice termination (on which the edge plasmon dispersion depends sensitively) and even the underlying bulk lattice (e.g. antidot shape, antidot size a/d, and lattice type).

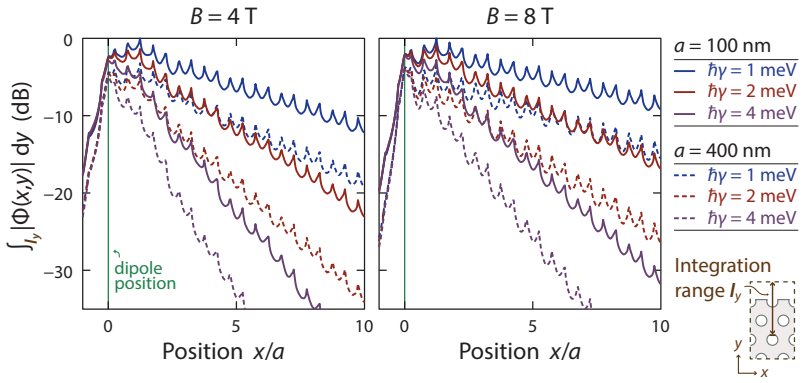

FIG. S9 Propagation attenuation (quantified by the y-integrated potential) of the $\bar{C}^{(1)} = -1$ gap edge plasmon, for varying decay rate $\hbar\gamma$, lattice constant a, and magnetic field B. By lowering a or increasing B the effective propagation length l/a can be increased dramatically. Edge plasmons are dipole-excited at the $\bar{C}^{(1)} = -1$ gap-center (14.6 and 29.2 THz at $a = 400$ and 100 nm, respectively). Setup parameters and (relative) dipole position as in Fig. 4(a); computational geometry as in Fig. S1. Matching time-domain calculations are included as Supplemental Movies.

To accompany the frequency-domain calculations in Figs. 4(e) and S9 we have also performed time-domain calculations.[13] The results (setup as in Fig. S9) are included as Supplemental Movies 1 and 2 and depict the induced potential due to a spectrally narrow (temporally broad) dipole pulse centered at the $\bar{C}^{(1)} = -1$ gap-center.

D. Effective Dirac Hamiltonian at the K point

Finally, we discuss briefly the spectral behavior of the $n = 1$ and 2 band near the $\mathbf{K}$ point, where the plasmonic bands exhibit Dirac dispersion. In the absence of $\mathcal{T}$ breaking perturbations (a magnetic field or intrinsic loss), the influence of small momentum deviations $\mathbf{\Delta k}$ from the $\mathbf{K}$ point can be well-described by a 2-component effective Dirac Hamiltonian $\Delta\hat{H}$, which gives the spectral shifts away from the Dirac point [i.e. the total effective Hamiltonian includes a diagonal term $\omega^0_{\mathbf{K}} \equiv \omega_1(\mathbf{K}) = \omega_2(\mathbf{K})$]. In the chiral representation, $\Delta\hat{H}$ takes the form

$$\Delta\hat{H} = \begin{pmatrix} 0 & v(\Delta k_x - \mathrm{i}\Delta k_y) \\ v(\Delta k_x + \mathrm{i}\Delta k_y) & 0 \end{pmatrix} = v(\Delta k_x \sigma_1 + \Delta k_y \sigma_2). \tag{S29}$$

Here, v is a linear phase velocity depending on E_F, a, and d. The two basis wavefunctions in this subspace are linear combinations of the original plane-wave states of $\tilde{\Phi}$, J_x, and J_y sampled over the wave vectors

[13] The time-domain formulation follows directly from the frequency-domain considerations in Section I, requiring only the substitution $-\mathrm{i}\omega \to \partial_t$; this leads to a third order ordinary differential equation [driven, for nonzero $\Phi^{\mathrm{ext}}(\mathbf{r}, t)$] which we propagate in time using an adaptive Runge–Kutta method.

$\{\mathbf{K}+\mathbf{G}\}$. They form the time-reversal counterpart of each other in the chiral representation.

If we next apply a finite magnetic field and finite loss, i.e. break $\mathcal{T}$, the linear degeneracy at $\mathbf{\Delta k}=\mathbf{0}$ is lifted. To leading order, the effective Hamiltonian generalizes to

$$\Delta\hat{H}=\begin{pmatrix}-\frac{\mathrm{i}}{2}\gamma+\alpha\omega_{\mathrm{c}} & v(\Delta k_x-\mathrm{i}\Delta k_y)\\ v(\Delta k_x+\mathrm{i}\Delta k_y) & -\frac{\mathrm{i}}{2}\gamma-\alpha\omega_{\mathrm{c}}\end{pmatrix}=-\tfrac{\mathrm{i}}{2}\gamma\sigma_0+v\Delta k_x\sigma_1+v\Delta k_y\sigma_2+\alpha\omega_{\mathrm{c}}\sigma_3, \tag{S30}$$

with $\alpha\equiv\xi(1-\mathrm{i}\gamma/2\omega_{\mathbf{K}}^0)$ introduced for brevity, cf. Eq. (S27), with ξ depending on the ratio a/d. The effective Hamiltonian produces the gapped Dirac spectrum $\Delta\omega=-\frac{\mathrm{i}}{2}\gamma\pm\sqrt{\alpha^2\omega_{\mathrm{c}}^2+v^2|\mathbf{\Delta k}|^2}$, with $\Delta\omega$ denoting the spectral shift from degenerate Dirac point $\omega_{\mathbf{K}}^0$. Evidently, $\alpha\omega_{\mathrm{c}}$ plays the role of a finite (complex) mass term in the Dirac equation.

References

* These authors contributed equally to this work;
dafeijin@berkeley.edu; tchr@mit.edu
† linglu@iphy.ac.cn
‡ xzhang@me.berkeley.edu

[S1] W. Wang, T. Christensen, A.-P. Jauho, K.S. Thygesen, M. Wubs, and N.A. Mortensen, *Plasmonic eigenmodes in individual and bow-tie graphene nanotriangles,* Sci. Rep. **5**, 9535 (2015).

[S2] T. Christensen, *From Classical to Quantum Plasmonics in Three and Two Dimensions* (Springer Theses, 2017).

[S3] V.P. Gusynin, S.G. Sharapov, and J.P. Carbotte, *Magneto-optical conductivity in graphene,* J. Phys.: Condens. Matter **19**, 026222 (2007).

[S4] A. Ferreira, N.M.R. Peres, and A.H. Castro Neto, *Confined magneto-optical waves in graphene,* Phys. Rev. B **85**, 205426 (2012).

[S5] I. Gohberg, P. Lancaster, and L. Rodman, *Matrix Polynomials* (SIAM, 2009).

[S6] P. Lancaster, I.N. Sneddon, M. Stark, and J.P. Kahane, *Lambda-matrices and Vibrating Systems*, 1st ed. (Pergamon Press, 1966).

[S7] J.E. Pask, B.M. Klein, P.A. Sterne, and C.Y. Fong, *Finite-element methods in electronic-structure theory,* Comput. Phys. Commun. **135**, 1 (2001).

[S8] D.R. Wilton, S.M. Rao, A.W. Glisson, D.H. Schaubert, O.M. Al-Bundak, and C.M. Butler, *Potential integrals for uniform and linear source distributions on polygonal and polyhedral domains,* IEEE Trans. Antennas Propag. **32**, 276 (1984).

[S9] J.M. Ziman, *Principles of the Theory of Solids*, 2nd ed. (Cambridge University Press, 1972).

[S10] B. Gallinet, A.M. Kern, and O.J.F. Martin, *Accurate and versatile modeling of electromagnetic scattering on periodic nanostructures with a surface integral approach,* JOSA A **27**, 2261 (2010).

[S11] D. Sun, J. Manges, X. Yuan, and Z. Cendes, *Spurious modes in finite-element methods,* IEEE Antennas Propag. Mag. **37**, 12 (1995).

[S12] S.M. Rao, D.R. Wilton, and A.W. Glisson, *Electromagnetic scattering by surfaces of arbitrary shape,* IEEE Trans. Antennas Propag. **30**, 409 (1982).

[S13] K.D. Ikramov, *Matrix pencils: theory, applications, and numerical methods,* J. Math. Sci. **64**, 783 (1993).

[S14] I.S. Gradshteyn and I.M. Ryzhik, *Table of Integrals, Series, and Products*, 7th ed. (Academic Press, 2007).

[S15] P. Wang, L. Lu, and K. Bertoldi, *Topological phononic crystals with one-way elastic edge waves,* Phys. Rev. Lett. **115**, 104302 (2015).

[S16] T. Fukui, Y. Hatsugai, and H. Suzuki, *Chern numbers in discretized Brillouin zone: Efficient method of computing (spin) Hall conductances,* J. Phys. Soc. Jpn. **74**, 1674 (2005).

[S17] A.H. Castro Neto, F. Guinea, N.M.R. Peres, K.S. Novoselov, and A.K. Geim, *The electronic properties of graphene,* Rev. Mod. Phys. **81**, 109 (2009).

[S18] O.L. Berman, G. Gumbs, and Y.E. Lozovik, *Magnetoplasmons in layered graphene structures,* Phys. Rev. B **78**, 085401 (2008).

[S19] R. Roldán, J.-N. Fuchs, and M.O. Goerbig, *Collective modes of doped graphene and a standard two-dimensional electron gas in a strong magnetic field: linear magnetoplasmons versus magnetoexcitons,* Phys. Rev. B **80**, 085408 (2009).